Composite Structures 363 (2025) 119135

Contents lists available at ScienceDirect

Composite Structures

journal homepage: www.elsevier.com/locate/compstruct

Improved online secondary path modelling for multiharmonic active vibration control in shape memory polymer composites

Weikai Shi [a], Xudong Zhang [a], Peilei Xu [a], Jianlong Gao [a], Pengxiang Zhao [a], Yaxiang Sun [b], Xin Lan [b,*], Jinsong Leng [b], Yanju Liu [a,*]

[a] Department of Astronautical Science and Mechanics, Harbin Institute of Technology, Harbin 150001, People's Republic of China
[b] Centre for Composite Materials and Structures, Harbin Institute of Technology, Harbin 150001, People's Republic of China

ARTICLE INFO

Keywords:
Active vibration control
Filtered-x least mean square
Shape memory composite
Macro fiber composite
Online secondary path modelling

ABSTRACT

This manuscript introduces a new approach to active vibration control (AVC), which involves the application of enhanced online secondary path modelling through a modified filtered-x least mean squares (FxLMS) algorithm. A special feature of this proposed control method is the use of an original adaptive variable step size (VSS) LMS algorithm to adjust the secondary path modelling filter. The adaptive step size is dynamically adjusted based on the modelling filter error signal, which is continuously monitored using a single exponential smoothing technique. The incorporation of the fractional derivative with the steepest descent method enhances the convergence speed of secondary path identification. Based on numerical simulations employing multilinear spectral and random vibration signals, the proposed method demonstrates advantages in convergence speed, system stability and model accuracy compared to typical existing algorithms. Specifically, the system modelling convergence rate is improved by 60 %, and the residual error convergence rate is improved by 72 %. In practical terms, the adaptive algorithm was implemented in shape memory polymer composites (SMPCs) to accommodate configuration variations. Employing multiharmonic AVC with macro fiber composite (MFC) actuators, the dynamic behavior and vibration control efficiency of SMPCs with varying carbon fiber volume fractions were subjected to comprehensive experiments and analyses. Results from the study showcase the efficacy of the proposed adaptive control strategy in significantly damping vibrations in both the original and bent shapes of SMPCs, suggesting the versatility and robustness of the control approach across different configurations. Meanwhile, this study provides support for vibration control of SMPCs in dynamic applications.

1. Introduction

Shape memory polymer composites (SMPCs), synthesized by incorporating carbon fibers with exceptional properties such as high strength, corrosion resistance and high-temperature endurance into shape memory polymers, have emerged as a revolutionary material solution in modern aerospace and other domains [1,2]. These composites not only demonstrate remarkable characteristics such as low density, significant deformability, programmable design, recoverability and easy molding but also enhance the mechanical strength through effective load transfer facilitated by the robust interfacial interactions between the carbon fibers and the matrix. In the aerospace sector, SMPCs have been extensively developed and researched for deployable structures such as hinges, trusses, antennas and morphing skins [3–5]. The deployability of these structures is crucial for deep-space exploration missions, as it significantly reduces the launch volume and weight of spacecraft, thereby lowering costs. This functionality of SMPCs predominantly derives from their ability to undergo pre-programmed shape changes under specific external stimuli, such as temperature, electric fields, magnetic fields, etc [6].

Deployable hinge structures fabricated from SMPCs have progressively found applications in spacecraft [7–9]. Current research predominantly focuses on the modification of the reinforcing phase and the matrix within SMPCs, as well as the design of the structures. However, there is limited research concerning the dynamic characteristics and AVC of SMPCs [10]. It is of great significance for in-depth studies that address the dynamic responses of SMPC-based systems under operational conditions typical in space missions. Exploring the dynamic properties and developing effective vibration control strategies are crucial for ensuring the functional integrity and operational reliability of these deployable structures in the challenging aerospace environment.

* Corresponding authors.
E-mail addresses: lanxin@hit.edu.cn (X. Lan), yj_liu@hit.edu.cn (Y. Liu).

https://doi.org/10.1016/j.compstruct.2025.119135
Received 8 August 2024; Received in revised form 14 February 2025; Accepted 25 March 2025
Available online 26 March 2025

Nomenclature

AVC	Active vibration control
FxLMS	Filtered-x least mean squares
VSS	Variable step size
SMPCs	Shape memory polymer composites
MFC	Macro fiber composite
PZT	Piezoelectric ceramic transducer
VARTM	Vacuum-Assisted Resin Transfer Molding
FRF	Frequency response function
FIR	Finite impulse response
WGN	White Gaussian noise
$x(n)$	Input signal
$x'(n)$	Filtered input signal
$y(n)$	Control output signal
$y'(n)$	Control signal after it passes through the secondary path
$d(n)$	Primary response
$e(n)$	Residual error signal
$f(n)$	Modelling error
$v(n)$	Zero-mean signal of white Gaussian noise
$v'(n)$	Undesired output resulting from $v(n)$ passing through $S(z)$
$v''(n)$	Convolution of $v(n)$ with the secondary path modelling filter
$P(z)$	Primary path filter
$W(z)$	Vibration control filter
$S(z)$	Secondary path filter
$S'(z)$	Secondary path modelling filter
L	Tap-weight lengths of $W(n)$
M	Tap-weight lengths of $S'(n)$
$\mu_s(n)$	Step size parameter of the secondary path modelling filter
μ_w	Step size parameter for the control filter
α	Forgetting factor
β	Updating factor
$J(n)$	Cost function
fr	The order of the fractional derivative
${}_aD_t^{fr}$	Grunwald–Letnikov definition of the fractional derivative
$\Gamma(\cdot)$	Gamma function
$R(n)$	Residual error of AVC system
$\Delta S(n)$	Relative modelling error of AVC system
σ^2	Variance of WGN
$Trans$	Transition temperature of SMPCs
θ	Bending angle of SMPCs
v_f	Fiber volume fraction
$w(x,y,t)$	Deflection function of the plate
∇^4	Biharmonic operator
ρ	Density of the material
h	Thickness of the plate
η_{mn}	Modal amplitude of the (m,n)-th mode
$\Phi_{mn}(x,y)$	Mode functions
ω_{mn}	Natural frequency of the (m,n)-th mode

Such research could significantly contribute to the optimization and enhanced performance of SMPCs in aerospace applications, ultimately leading to more robust and efficient spacecraft designs. Given that SMPC structures in practical applications are subject to various dynamic disturbances, including but not limited to spacecraft maneuvers, space radiation pressure, microwave radiation and gravity gradient torques, vibration control becomes a critical technical challenge. These disturbances can induce vibrations that may affect the normal functioning of the structures [11]. In this context, employing adaptive control strategies, such as the FxLMS algorithm with online secondary path identification, offers a unique advantage. This approach can adjust the control signal output in real-time based on changes in the external environment and the performance of the control system, effectively suppressing vibrations and ensuring the stability and reliability of the SMPC structures, all without the need for establishing complex mechanical models.

For engineering structures, the resonance and reduced lifespan caused by vibration must be accounted for [12–14]. Vibration characteristics are crucial when assessing the dependability of structures and their systems [15–18]. Piezoelectric smart materials enable the integration of sensors, controllers and actuators, making active vibration control systems based on these smart materials intelligent, lightweight and miniaturized. Active vibration control using piezoelectric materials has emerged as a key area of interest in the field of engineering [19–25]. To utilize piezoelectric technology for active structural vibration control, active control strategies must be applied [11,26,27]. The FxLMS adaptive algorithm is a prevalently used control algorithm for AVC systems based on piezoelectric intelligent structures. It provides several benefits, including a positive control effect, ease of implementation and the ability to manage multiple-input multiple-output systems. The pioneering work of Elliott et al. marked the introduction of a vibration controller based on the LMS algorithm, which yielded impressive outcomes in effectively suppressing vibrations [28]. Oh et al. conducted research employing the FxLMS algorithm to mitigate the vibrations of a flexible beam with a bonded PZT actuator experiencing sinusoidal and white noise disruptions [29]. The FxLMS algorithm is being progressively developed and applied within the engineering field, building upon prior research efforts. Niu et al. devised a refined FxLMS algorithm based on existing signals to identify secondary paths. Through numerical simulations and experiments on vertical tail buffeting control, this algorithm has proven to be advantageous for adaptive vibration control of dynamic structures [22]. Meng et al. developed a feedforward adaptive method for AVC applied to a helicopter fuselage structure that incorporates the use of piezoelectric stack actuators. The effectiveness of this technique was confirmed through both simulations and AVC experiments [30,31]. However, the traditional FxLMS algorithm exhibits a tradeoff between the rate of convergence and the efficacy of vibration suppression [32,33].

The FxLMS algorithm is a frequently employed adaptive algorithm within AVC systems [34,35], and its control block diagram is shown in Fig. 1. In the system, a sensor collects the input signal $x(n)$, while another sensor detects the residual vibration $e(n)$, and an actuator transmits the control signal $y(n)$, which is calculated by the vibration control filter $W(z)$. Before undergoing weight updating through the LMS algorithm, $x(n)$ undergoes secondary path compensation, in which it is filtered by an estimated $S'(z)$ to counteract secondary path effects. The

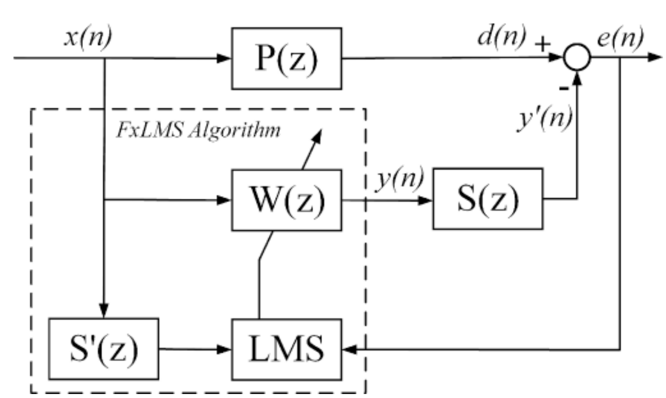

Fig. 1. FxLMS algorithm based AVC system.

FxLMS algorithm demonstrates robustness in the identification of the secondary path in the presence of errors [36].

Two methods exist for identifying secondary paths: offline identification and online identification. Offline identification, which is simpler in nature, only necessitates experimental identification of the secondary paths before the AVC system is operational. Nonetheless, the existence of fixed modelling errors may cause the FxLMS algorithm to converge slowly and cause a steady-state bias [37]. In contrast, online identification can promptly compensate for modelling errors while continuously monitoring secondary path changes that may occur due to factors such as component ageing, thermal fluctuations, and environmental changes [38,39]. The online identification of secondary paths can be further divided into two methods. The first method involves directly modelling the secondary path based on its input $y(n)$ and output signals $y'(n)$. The second approach entails injecting an additional random signal into the AVC system and then designing the identification method for modelling purposes [40–46]. A comprehensive analysis of the above two approaches is presented in [47], which leads to the conclusion that the second approach surpasses the first in terms of the convergence rate, duration of updates, responsiveness to primary signal fluctuations, computational complexities and other factors. Thus, this study selects the second identification method as the research focus.

The basic additive random noise technique was first proposed by Eriksson et al. [48]. In the AVC system, as shown in Fig. 2 (a), a subsystem that integrates an adaptive filter is introduced into the conventional FxLMS system for online identification of the secondary path. However, the white noise signal introduced into this subsystem passes through the secondary path, influencing the residual error signal. This influence can impact the convergence and efficacy of the control link, particularly during its convergence phase. As the control link converges, the white noise component within the residual error signal interacts with the control filter output signal, potentially introducing errors or oscillations into the control filter as it approaches convergence. Moreover, systematic residual errors in the control phase output are also utilized in the identification phase, leading to mutual interference between these processes that further degrades the overall performance of the AVC system. Therefore, when designing a subsystem for secondary path identification, the sensitivity of the control link to white noise signals must be considered. The impact of the white noise power on the design of the control filter, system stability and secondary path identification accuracy must be comprehensively evaluated to ensure effective identification and control.

In [41–43], white noise is eliminated from the residual error signal by introducing a third filter based on Eriksson's method. The simulation results presented in [43] demonstrate that their proposed method produces superior results to those of prior methods. However, notably, the inclusion of the third filter increases the complexity and computational load of the system design. Akhtar et al. improved the performance of the AVC system by employing only two adaptive filters [49]. As demonstrated in Fig. 2 (b), the step size of the modelling filter is dynamically adjusted within specified upper and lower limits. This VSS implementation is grounded in the principle that the estimation error gradually diminishes and ideally converges to zero. Compared with that of the Eriksson method, the upper limit of the step size parameter is greater, leading to faster convergence with the increase in the step size. Aslam et al. proposed a novel VSS algorithm for identifying the secondary path [46]. As depicted in Fig. 2 (c), the step size undergoes multidirectional variations in relation to the modelling error $f(n)$. This is a departure from the algorithms proposed in [49–54], where the step size parameter starts low and gradually increases to the upper value, facilitating rapid convergence. Subsequently, as the modelling error diminishes, the step parameter decreases to enhance the system stability. Fractional LMS was introduced to improve the convergence and increase the robustness of the system.

The typical approaches mentioned above come with a tradeoff between accurate secondary path identification and rapid convergence [55]. Inspired by the Aslam method, this manuscript presents a novel approach for AVC systems. As depicted in Fig. 3, the control filter is adjusted by employing the simple LMS algorithm to improve the control speed and achieve rapid convergence. In the modelling process, the step size is determined by combining the power and value of the residual error signal, showing an innovative relationship with the cube of $f(n)$. This VSS strategy significantly differs from other existing VSS algorithms that demonstrate improved speed and convergence, without the need for a third adaptive filter or an additional control filter. Based on the obtained FxLMS algorithm with modified multidirectional VSS fractional derivative LMS for online secondary path modelling, AVC simulations are conducted in this study to compare the proposed method with classical approaches, considering both external excitation variations (alterations in the amplitude, phase, and frequency of vibration signals, along with superimposed measurement noise) and internal path variations (simulating the reduced secondary path response due to actuator performance degradation). These investigations are designed to validate the superiority and adaptability of the proposed method. Additionally, this study explores the AVC of SMPCs in two distinct operational states: the original shape and the bent shape. The research aims to understand how the dynamic characteristics and control effectiveness of SMPCs are influenced by their shape and the carbon fiber volume fraction. By employing the proposed adaptive control strategy with MFC, the study evaluates the performance of vibration control in both shapes and identifies the challenges posed by shape deformation. This research contributes to the development of advanced control strategies for SMPCs, providing significant theoretical support and technical guidance that enhance their applicability in various engineering fields.

The innovations of this paper are reflected in the following aspects:

(1) Innovative algorithm application: This study introduces an adaptive multidirectional VSS control algorithm combined with an online secondary path identification strategy, significantly

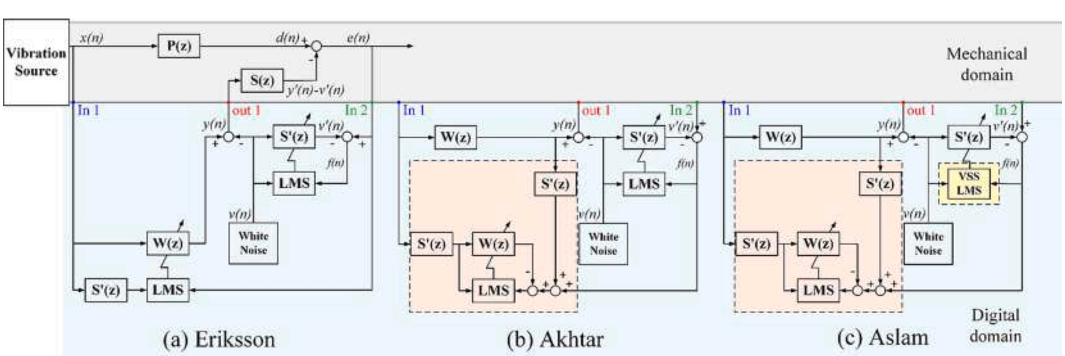

Fig. 2. FxLMS algorithm based AVC system with online secondary path modelling: (a) Eriksson method, (b) Akhtar method, and (c) Aslam method.

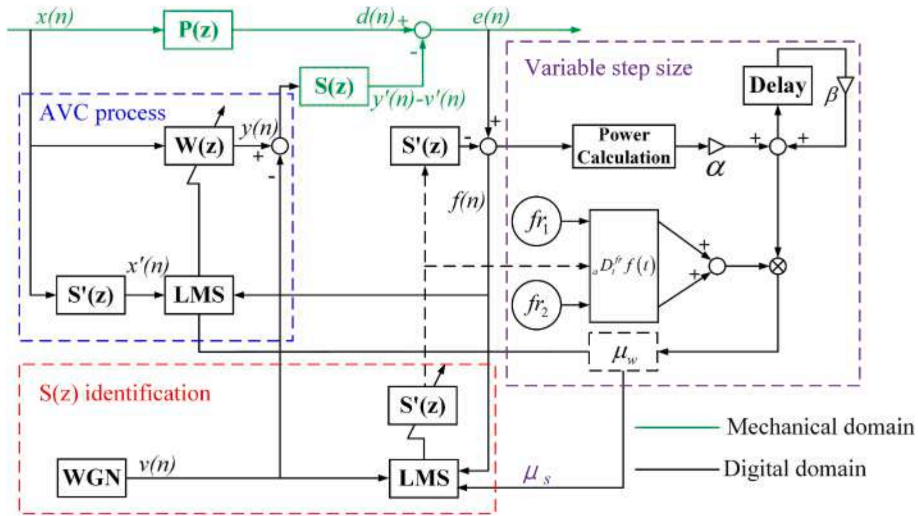

Fig. 3. Proposed AVC system with online secondary modelling.

enhancing convergence speed, modelling accuracy and system response in complex environments.

(2) Dynamic response and robustness analysis: We demonstrated the high adaptability and robustness of the control system under various excitations and secondary paths, ensuring effective vibration mitigation. An in-depth analysis of the dynamic responses of SMPCs in different configurations was conducted, revealing their performance under typical operational conditions of space missions, providing new insights for future material design and optimization.

(3) Application and experimental validation: The control algorithm was successfully applied to SMPCs in various configurations, effectively reducing vibrations. A series of multiharmonic vibration control experiments using MFC were conducted, validating the proposed method's effectiveness and feasibility in dynamic environments, thus providing empirical support for subsequent technology dissemination and application.

2. Proposed method

In this section, we present a novel approach to AVC by introducing an adaptive filtering framework. The proposed method leverages dynamic step-size adjustments, multidirectional VSS strategies, and fractional-order calculus to enhance the convergence speed, stability and accuracy of the AVC system. The subsections are structured as follows: Subsection 2.1 outlines the adaptive filter iteration process and fundamental principles behind the proposed method, detailing the interaction between the control filter and secondary path. Subsection 2.2 introduces a multidirectional VSS strategy, which ensures adaptive and robust parameter tuning for optimal system performance. Subsection 2.3 explores the integration of fractional derivatives into the LMS algorithm, demonstrating how this technique enhances modelling precision and the ability to handle complex system dynamics.

2.1. Adaptive filter iteration for the proposed method

Fig. 3 shows the basic principle block diagram of the proposed method. In this system, $W(z)$ represents the control filter, specifically, a finite impulse response (FIR) filter with a tap-weight length of L. The resulting output, $y(n)$, generated by the input signal $x(n)$ after it passes through $W(z)$ can be expressed as:

$$y(n) = W^T(n)x_L(n) \tag{1}$$

where $W(n) = [w_0(n)w_1(n)\cdots w_{L-1}(n)]^T$ and $x_L(n) = [x(n)x(n-1)\cdots x(n-L+1)]^T$ are $L-$sample vectors. A zero-mean signal of white Gaussian noise (WGN), denoted as $v(n)$, is introduced into the output $y(n)$. Consequently, the residual error signal $e(n)$ can be expressed as:

$$e(n) = d(n) - y'(n) + v'(n) \tag{2}$$

where $d(n) = P(n) * x(n)$ represents the primary response of the AVC system, $y'(n) = S(n) * y(n)$ is the output of the control signal $y(n)$ after it passes through the secondary path $S(z)$, and $v'(n) = S(n) * v(n)$ represents the undesired output resulting from $v(n)$ passing through $S(z)$.

The convolution of $v(n)$ with the secondary path modelling filter $S'(z)$ is defined as $v''(n)$:

$$v''(n) = S'^T(n)v(n) \tag{3}$$

where $S'(n) = [s'_0(n)s'_1(n)\cdots s'_{M-1}(n)]^T$ and $v(n) = [v(n)v(n-1)\cdots v(n-M+1)]^T$ are $M-$sample vectors. Then, $v''(n)$ is subtracted from $e(n)$ to obtain the error signal $f(n)$:

$$f(n) = e(n) - v''(n) \tag{4}$$

Hence, the tap weights of $S'(z)$ can be adjusted according to the following procedure:

$$S'(n+1) = S'(n) + 2\mu_S(n)f(n)v(n) \tag{5}$$

Here, $\mu_s(n)$ represents the step size parameter of the secondary path modelling filter. Note that the step size depends on time, which will be further explained in the subsequent subsection.

Meanwhile, the tap weights of $W(z)$ are adjusted as follows:

$$W(n+1) = W(n) + 2\mu_w f(n)x'(n) \tag{6}$$

where $x'(n) = S'^T x_M(n)$ denotes the filtered input signal vector for $W(z)$ and $x_M(n) = [x(n)x(n-1)\cdots x(n-M+1)]^T$ represents an $M-$sample vector. μ_w represents the step size parameter for the control filter. Following the update of the tap weights, the control filter generates a corresponding signal intended for transmission through the secondary path, prompting it to produce a signal aimed at suppressing system vibration responses.

2.2. Multidirectional VSS strategy of the modelling filter

Based on Eqs. (2) and (4), $f(n)$ consists of two components: $d(n) - y'(n)$ and $v'(n)$ - $v''(n)$. The first component significantly interferes with the modelling process, seriously affecting the estimation accuracy of the modelling filter and leading to potential instability in the AVC system due to its initially large value. However, as the number of tap-weight iterations increases, the influence of this component gradually diminishes. Therefore, it is advisable to initially set the step size parameter $\mu_s(n)$ to a small value. Subsequently, as the disturbance signal decreases, it is suggested to increase the parameter value. Hence, the step size is determined by combining the power and amplitude of the error signal, showing an innovative relationship with the cube of $f(n)$. A mechanism for adjusting $\mu_s(n)$ can be formulated as:

$$\mu_s(n) = \left[\alpha\mu_s(n-1) + \beta f^3(n)\right]\mu_w \tag{7}$$

where α and β are constants that specify a multidirectional varied step size function, and the initial value of $\mu_s(n)$ is 0.

The choice of Eq. (7) for $\mu_s(n)$ is justified by the fact that the step size is increased from zero by setting the values of α and β in the initial stage of the AVC system adaptation, during which the system residual error and the path estimation error are rapidly reduced. Subsequently, the step size for tracking the error signal gradually decreases, and a decreased step size is employed to improve the modelling accuracy, enhance the system stability and minimize fluctuations.

2.3. Fractional derivative LMS algorithm

Fractional derivatives are more flexible in handling signals and systems with complex characteristics, including nonsmoothness, singularities or multiscale behaviour. Their ability to capture long-term correlations due to their longer memory is crucial for modelling systems with such characteristics. This makes them a valuable tool for understanding and analysing various real-world phenomena and processes. In the past three decades, fractional differentiation and integration have been extensively applied across various fields, demonstrating the broad and diverse practical utility of fractional calculus. The incorporation of fractional derivatives within LMS algorithms has garnered considerable attention in the research community [56–59].

For fractional LMS algorithms, the fundamental principle involves determining the filter tap weights by computing the partial derivatives of the fractional order with respect to each element within the filter vector. This process also involves minimizing the cost function utilizing the steepest descent method, where the cost function corresponds to the mean square error:

$$J(n) = E[f(n)f^*(n)] = E\left[|f(n)|^2\right] \tag{8}$$

Here, $f(n)$ is defined by Eq. (4). Combining the first and fractional-order derivatives, the adaptive expression for $S'(n)$ is expressed as:

$$S'(n+1) = S'(n) - \mu_s\left(\frac{\partial J}{\partial S'}(n) + \frac{\partial^{fr} J}{\partial S'^{fr}}(n)\right) \tag{9}$$

where fr represents the order of the fractional derivative. Various expressions for fractional integrals and derivatives can be found in the literature [56–58]. The Grunwald–Letnikov definition of the fractional derivative ${}_aD_t^{fr}$ of order fr with a lower terminal at a for the function $f(t)$ is provided as [59]:

$${}_aD_t^{fr} f(t) = \lim_{h\to 0} h^{fr} \sum_{m=0}^{\infty} (-1)^m \binom{fr}{m} f(t + (fr - m)h) \tag{10}$$

Introducing $f(t) = t^n$ into the above expression:

$${}_aD_t^{fr} t^n = \frac{\Gamma(n+1)}{\Gamma(n - fr + 1)} t^{n-fr}, n > -1 \tag{11}$$

Upon incorporation of the fractional-order derivative term $\frac{\partial^{fr} J}{\partial S'^{fr}}(n)$ from Eq. (9) into Eq. (11) and subsequent simplification of it along with the first-order derivative term $\frac{\partial J}{\partial S'}(n)$, a conclusive iterative relationship for the tap weights of the modelling filter can be established:

$$S'(n+1) = S'(n) + 2\left[1 + \frac{|S'(n)|^{(1-fr)}}{\Gamma(2 - fr)}\right]\mu_s(n) f(n) v(n) \tag{12}$$

Absolute values are applied to filter coefficient vectors to prevent negative exponents. Additionally, $\Gamma(\cdot)$ represents the gamma function:

$$\Gamma(t) = \int_0^{\infty} x^{t-1} e^{-x} dx \tag{13}$$

3. Simulations and results

In this section, we evaluate the efficiency and adaptability of four methods through numerical simulations and performance comparisons, focusing on the proposed approach that enhances vibration suppression speed and stability by dynamically adjusting parameters and optimizing computational complexity. Initially, we compare computational efficiency, highlighting how the proposed method reduces complexity while maintaining efficiency across various filter lengths. Subsequently, we assess the performance of these methods by examining path identification speed, error and convergence speed, revealing the proposed method's significant advantages in accuracy and convergence. Finally, we present AVC simulations in dynamic environments, demonstrating the robustness and efficiency of the proposed method by altering external excitation and path parameters.

3.1. Comparison of the computational efficiency

The computational complexity of an algorithm is often assessed by considering the number of computations executed per iteration. This evaluation provides insights into the efficiency and resource requirements of the algorithm, which are crucial for assessing its practical implementation in real-world scenarios [41]. Table 1 details a comparative analysis of the computational complexities of the proposed method and three conventional methods. In this context, Eriksson represents Eriksson's method from [40], Akhtar corresponds to Akhtar's method from [45], and Aslam signifies Aslam's method from [46]. Additionally, L and M correspond to the tap-weight lengths of $W(n)$ and $S'(n)$, respectively. While it shares similarities with Aslam's method, the proposed approach stands out by leveraging the variation in the system parameters and consolidating the step size of both integer and fractional-order derivatives. This consolidation notably diminishes the number of controller parameters and enhances the overall efficiency. Furthermore, the computational efficiency of the proposed method is similar to that of Akhtar's method (as depicted in Fig. 4, showing a region where the computational complexities of both Akhtar's method and the proposed method are lower across various filter tap-weight lengths), although it marginally surpasses that of Eriksson's method. Reducing computational complexity is often a significant goal in algorithm design.

Table 1
Comparison of the computational efficiency of different methods.

Method	Additions	Multiplications	Additions ($L = M$)	Multiplications ($L = M$)
Eriksson	$2L + 3M$-1	$2L + 3M + 2$	$5L$-1	$5L + 2$
Akhtar	$3L + 4M + 5$	$3L + 4M + 10$	$7L + 5$	$7L + 10$
Aslam	$3L + 5M + 6$	$3L + 5M + 13$	$8L + 6$	$8L + 13$
Proposed	$2L + 5M + 9$	$2L + 4M + 18$	$7L + 9$	$6L + 18$

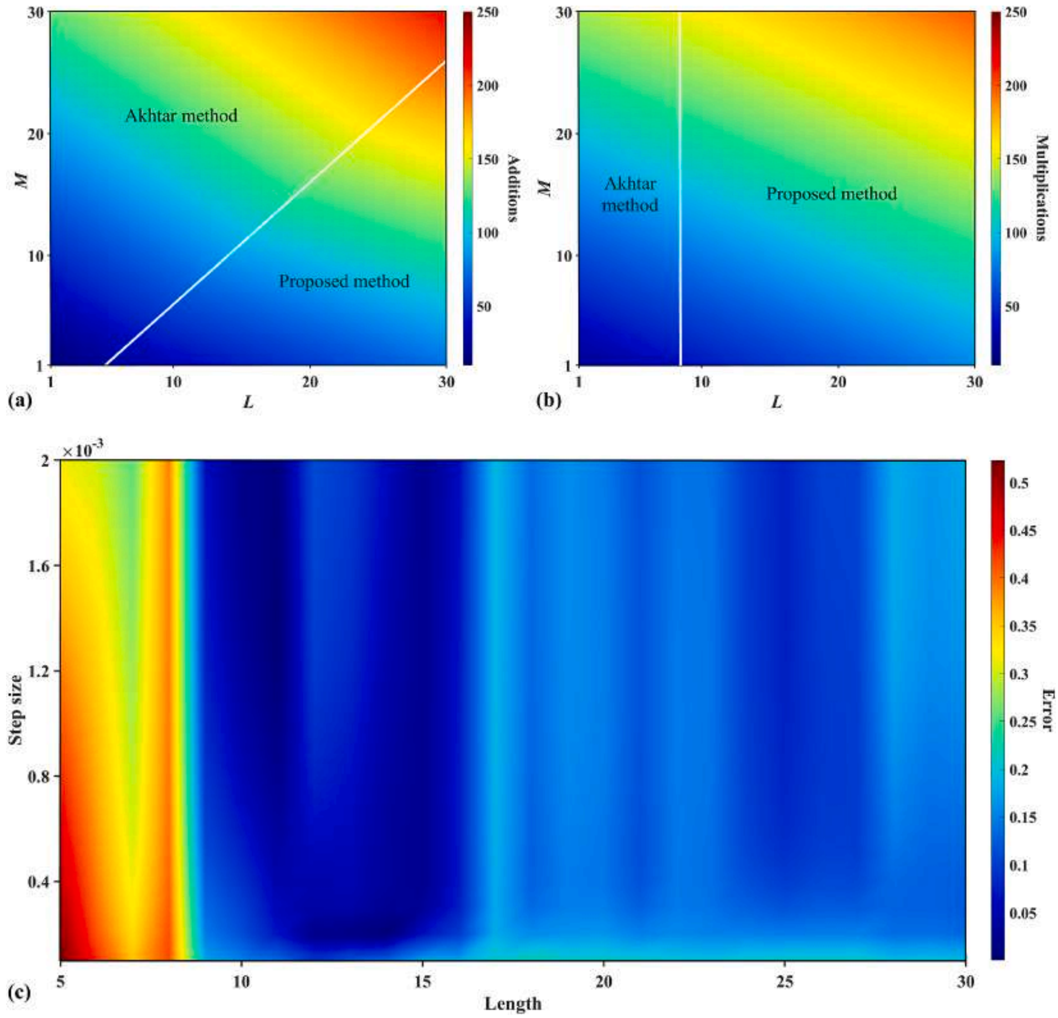

Fig. 4. The regions formed by the smaller computational complexity of the Akhtar method and proposed method for different L and M: (a) additions and (b) multiplications, (c) residual error of the proposed controller with different step size and length.

The next section will show that the proposed approach strikes a balance between complexity and performance. The adjustment of the tap-weight length and step size of $W(n)$, as depicted in Fig. 4 (c), shows the residual error of the system. When the controller step size changes, the error remains small when the length is set to 10 or 15. Considering the computational complexity of the controller as shown in Fig. 4 (a) and (b), it was decided that for subsequent controllers, the tap-weight length would be set to 10. This decision balances the need for effective control with the practical constraints of computational resources and implementation complexity.

3.2. Performance comparison of the four methods

This part compares the performances of the four methods through numerical simulation. The performance of these methods is evaluated in terms of the path identification speed and error and the vibration suppression signal convergence speed and results. Here, two key parameters are defined: the residual error and the relative modelling error, denoted as $R(dB)$ and $\Delta S(dB)$, respectively:

$$R(n) = -20\lg\frac{e(n)}{d(n)} \tag{14}$$

$$\Delta S(n) = 10\lg\left\{\frac{|S(n) - S'(n)|^2}{|S(n)|^2}\right\} \tag{15}$$

A smaller $R(n)$ signifies improved vibration control of the system, whereas a smaller $\Delta S(n)$ indicates more precise identification of secondary paths.

Numerical simulation programs are implemented for Eriksson, Akhtar and Aslam based on the methods described in the references [45,46,48]. These are then compared with the proposed method. Both the control filter and the modelling filter have a tap-weight length of 16 and are initialized with null vectors. The coefficients of $P(z)$ and $S(z)$ are [0.050–0.001 0.001 0.800 0.600–0.200–0.500–0.100 0.400–0.050] and [0.050–0.010 0.950 0.010–0.900], respectively. Their frequency response functions are shown in Fig. 5. The number of iterations is 40000. The input signal consists of WGN with a variance of 1.00. During the modelling process, WGN with a variance of 0.01 is incorporated to efficiently minimize the noise of the residual error once the system converges. Considering that system stability and convergence are contradictory, the step size of the control filter is determined as a constraint based on the criterion that the variance of the residual error after stabilization is less than 1.50, and the same parameters in different algorithms are maintained at the same value for performance comparison. The parameters are optimized through a trial-and-error process to attain swift, stable and enhanced performance, and their respective values are detailed in Table 2.

Fig. 6 shows the numerical simulation results. Upon closer examination of the modelling error curves in Fig. 6 (b), the Eriksson method clearly displays a slower convergence rate, whereas the Akhtar method

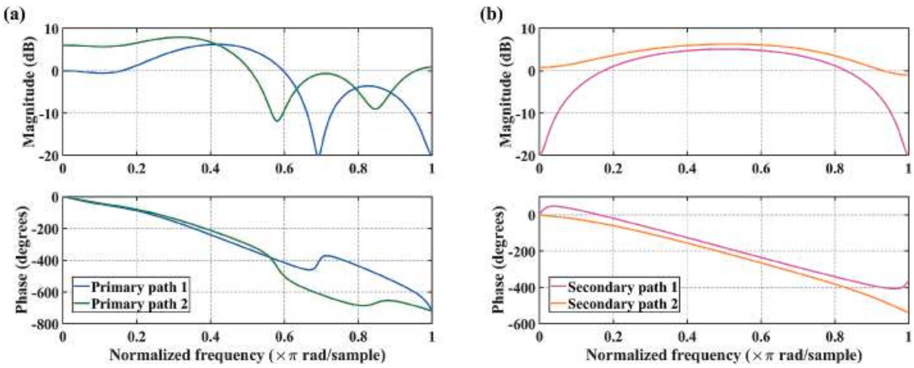

Fig. 5. Frequency response function of (a) the primary and (b) secondary paths used in the simulations.

Table 2
Parameter values used in the simulation.

Method	Parameters	Values
Eriksson	μ_w	0.0015
	μ_s	0.0070
Akhtar	μ_w	0.0015
	γ	0.9996
	$\mu_{s_{\min}}$	0.0080
	$\mu_{s_{\max}}$	0.0600
Aslam	μ_w	0.0015
	γ	0.9996
	$\mu_{1_{\min}}$	0.0080
	$\mu_{1_{\max}}$	0.0600
	$\mu_{s_{\max}}$	0.0200
	$\mu_{f_{\max}}$	0.0200
	α	0.9996
	β	0.0002
	fr	0.8
	A	1.0
	C_1	2.0
	C_2	1.0
Proposed	μ_w	0.0015
	α	0.9996
	β	0.0002
	fr	0.8

reaches convergence at approximately n = 15000 but then experiences substantial instability. The Aslam method appears to demonstrate better performance; however, the proposed method achieves a more rapid reduction in the modelling error than the previous methods. The optimal modelling error among the existing methods stabilizes at −30 dB around n = 12500. In contrast, for the proposed method, the same level of accuracy is attained at approximately n = 5000, representing a 60 % improvement in the convergence rate. Fig. 6 (a) and Fig. 6 (c) show the curves for the step size parameters and signal reduction, respectively. Fig. 6 (d) demonstrates that the residual error convergence rates of the previous approaches are nearly identical, with a stable-state value of −15 dB. The proposed method, on the other hand, becomes stable at approximately n = 1400, achieving the same value. Compared to the other methods that converge at approximately n = 5000, the proposed method boosts the residual error convergence rate by 72 %. Fig. 6 (a) clearly shows that in the initial stages, the values increase from a small quantity to accelerate convergence, after which the values decrease to account for misadjustments. Consequently, the general performance of the system is enhanced.

Then, we consider the case involving alterations to the primary and secondary paths while keeping the reference signal and controller parameters unchanged. At n = 20000, the paths change to as shown by green curves in Fig. 5, the performance of all the methods changes, as shown in Fig. 7. Fig. 7 (a) displays the variation in the step size parameter. Fig. 7 (b) clearly demonstrates that Eriksson's response shows no improvement following the alteration in the primary and secondary paths. In contrast, the proposed method, along with Akhtar's and Aslam's methods, adapts to the alteration, achieving a consistently high level of accuracy at a similar rate as that observed before the alteration. In particular, the superior modelling accuracy and faster convergence rate of the proposed method post-alteration show its adaptability and efficiency in dynamic environments. Notably, the signal attenuation performance appears to be very similar across all the methods, as demonstrated in Fig. 7 (c) and (d). All the methods clearly have the same final residual error control result of approximately −13 dB, but the proposed method still achieves the final control outcome very quickly after alteration of the primary and secondary paths.

3.3. AVC simulation of the four methods

The control block diagram was built according to the proposed strategy. AVC simulations were carried out under identical operating conditions, where the primary and secondary paths were obtained by offline identification: [147.47 982.31 922.42 –608.48 –1987.00 –2303.00 –806.40 1148.00 2576.00 3240.00] and [-14.56 68.22 –158.94 222.12 –177.20 38.32 57.99 –3.68 –119.89 116.18], respectively. The external excitation comprises multiple harmonics at frequencies of 10, 20 and 40 Hz, accompanied by a superimposition of 20 dB white Gaussian noise with a variance σ^2 set to 1E-4. To compare the convergence rates of the four methods, all the control filter weight coefficients were set to 5E-12. According to the four methods developed for multilinear spectral vibration signal control, a simulation of 60 s was performed. The system response is depicted in Fig. 8. The time-domain diagram reveals that the proposed method achieves the swiftest control speed, requiring only 0.1 s to accomplish vibration suppression. In contrast, the Eriksson, Akhtar and Aslam methods require approximately 5 s, 5 s and 1 s, respectively. Compared with the best method, the improved method enhances the control speed by 90 %, resulting in an approximate 80 % amplitude reduction. The frequency-domain diagram confirms that all four methods perform satisfactorily. The four methods ultimately achieve good control results. The three line spectrum are specifically reduced by 24.20 dB, 20.58 dB and 15.01 dB, respectively. Additionally, an attenuation effect surpassing 20 dB is demonstrated for the low-frequency noise component spanning 0–100 Hz.

This part presents an adaptive simulation of the proposed method, maintaining consistency in the input signal and controller parameters, as detailed in the preceding section. The external excitation modification involves amplifying the external excitation amplitude to twice the original value at the 10th second, altering the frequency to 60 Hz, 80 Hz and 100 Hz at the 20th second, and increasing the phase by a signal delay of 0.01 s at the 30th second. The variation in the secondary path is

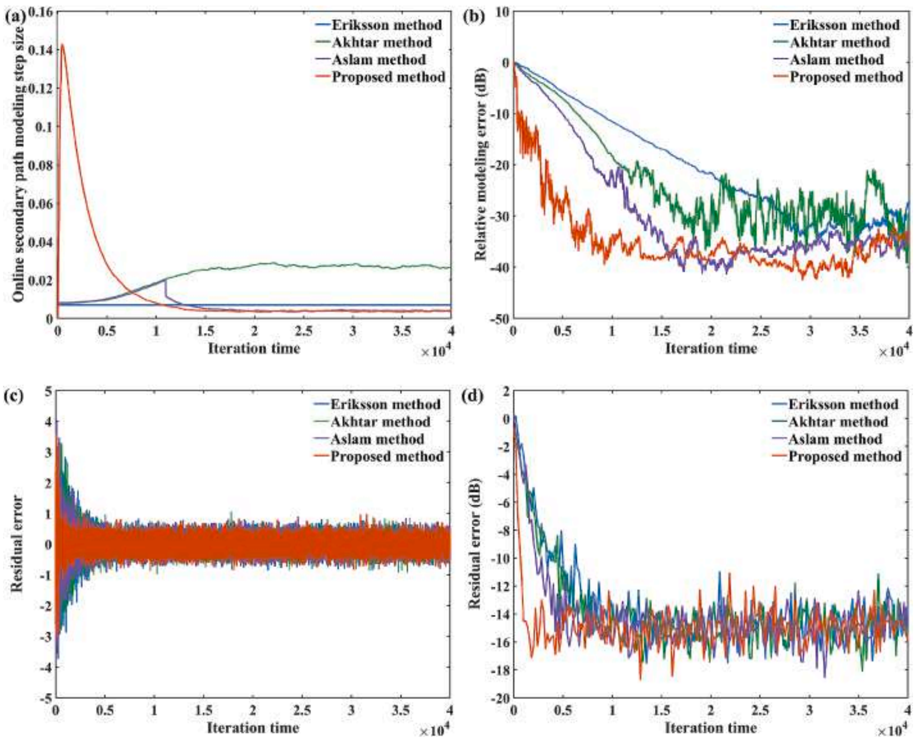

Fig. 6. Performance comparison of proposed method with previous methods (without paths alterations): (a) Online secondary path modelling step size, (b) relative modelling error, (c) residual error and (d) residual error envelop.

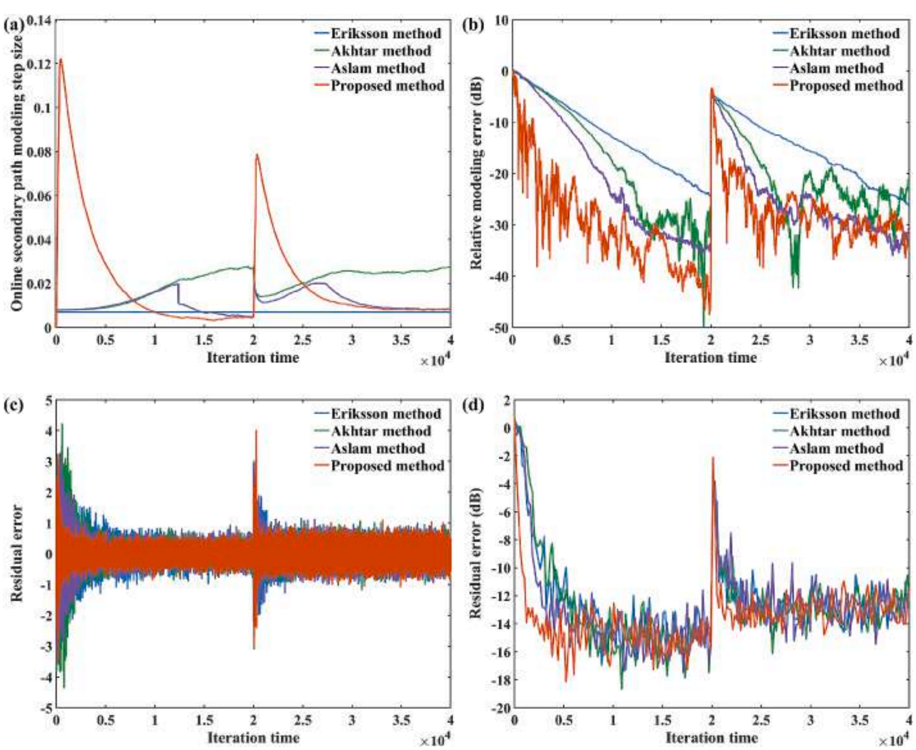

Fig. 7. Performance comparison of proposed method with previous methods (with paths alterations): (a) Online secondary path modelling step size, (b) relative modelling error, (c) residual error and (d) residual error envelop.

established as the coefficients being multiplied by 0.9 at 10 s, the coefficients being multiplied by 0.8 at 20 s, and the coefficients being multiplied by 0.7 at 30 s. The force response, controller output voltage, line spectral power and residual error reduction are depicted in the following diagrams.

Fig. 9 (a) and (b) indicates that alterations in the amplitude, frequency or phase of the external excitation prompt a rapid increase in the structural vibration response. During this period, the controller promptly adapts its output voltage in response to counteract the changes, subsequently resulting in a decay in the response. Fig. 9 (c)

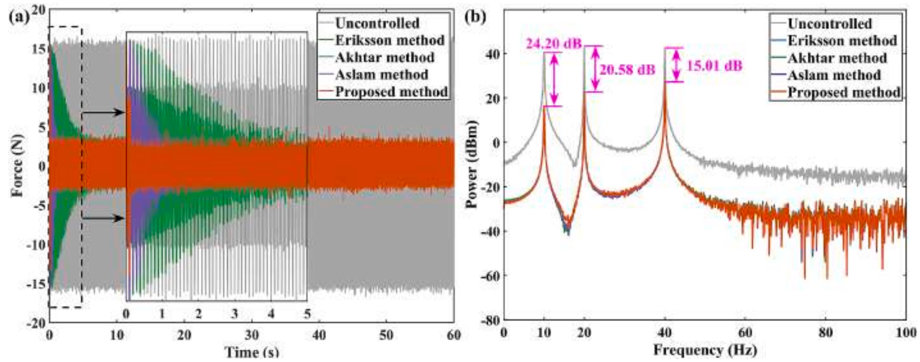

Fig. 8. The simulation results of AVI. (a) Time-domain and (b) frequency-domain.

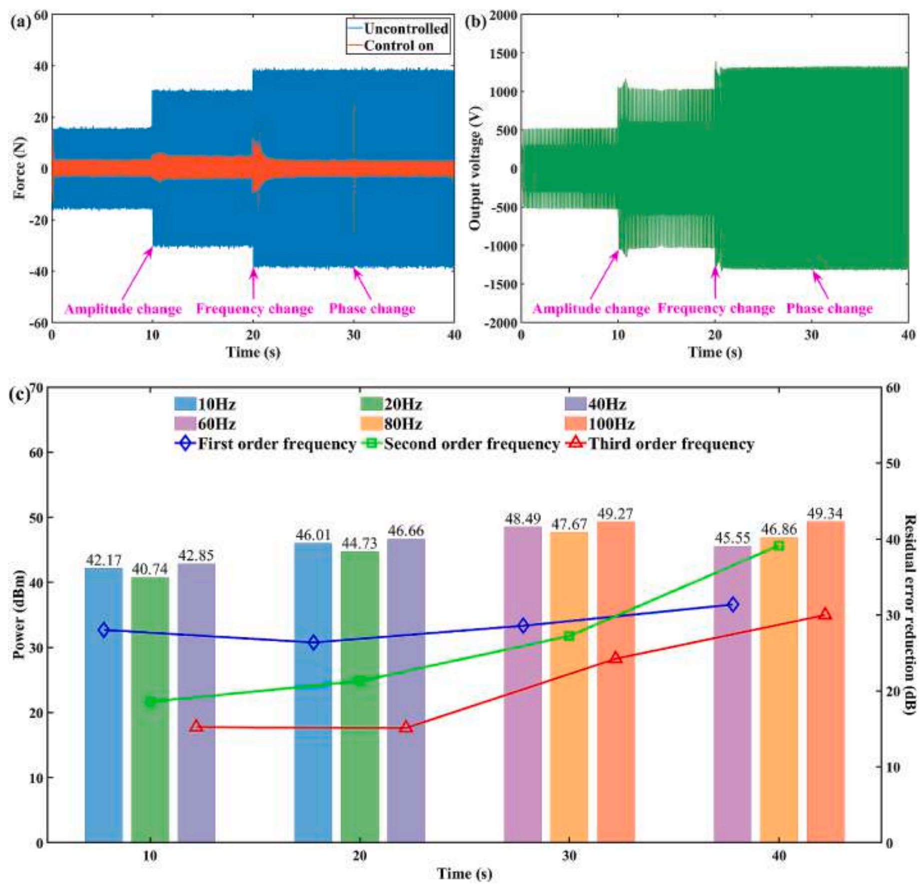

Fig. 9. Adaptability examination results of the proposed controller with the external amplitude, frequency and phase changing: (a) force response, (b) output voltage of the controller, (c) line spectral power and its residual error reduction change.

shows the power of each line spectrum (bar graph) and the corresponding reduction values (line graph) at four different moments of external excitation changes. The blue, green and red lines represent the suppression trends of the 1st, 2nd and 3rd order frequency signals, respectively. It can be observed that regardless of the changes in external excitation, the system's suppression effect on the vibration signals improves over time. This is due to the controller's gradual convergence in frequency demodulation of the input signals. Fig. 10 (a) and (b) shows that the structure vibration response remains almost constant when the secondary path changes. However, the controller can still fine tune the output voltage to suppress the response. Fig. 10 (c) shows that the changes in the secondary path have minimal impact on the power of each line spectrum of the signal, indicating that the system control is relatively stable. From Fig. 11 (a) and (b), it is evident that the vibration response of the structure significantly changes when there are simultaneous variations in the external excitation and the secondary path. Despite the complexity of this situation, the controller can promptly modify the output voltage to effectively regulate the system response. This demonstrates the robust adaptability of the proposed controller. Fig. 11 (c) shows that the line spectrum of the first-order frequency is mainly affected by the secondary path, and its trend is consistent with the second condition. The second-order and third-order line spectrum are less sensitive to changes in the secondary path, so the changes in these two lines are consistent with the first condition. Overall, regardless of changes in external excitation or internal path variations, the impact on the control effectiveness of multilinear spectrum is limited. The controller is able to respond promptly to changes and effectively reduce the power of multilinear spectrum.

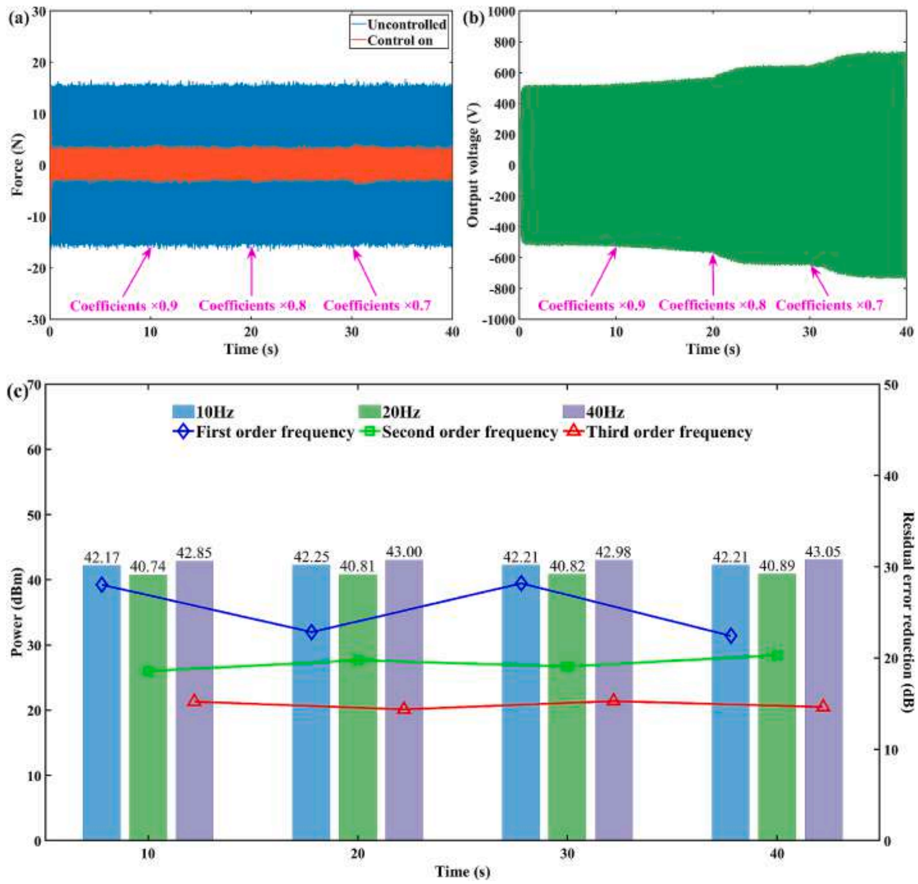

Fig. 10. Adaptability examination results of the proposed controller with the internal secondary path changing: (a) force response, (b) output voltage of the controller, (c) line spectral power and its residual error reduction change.

This chapter demonstrates the advantages of the proposed method in terms of computational efficiency, convergence speed and adaptability through detailed numerical simulations and performance comparisons. The results indicate that the proposed method outperforms others in vibration suppression speed and exhibits strong adaptability and effective control of vibration response under external excitations and internal physical channel variations. This designed adaptive control algorithm with online identification of secondary paths can track performance changes in actuators due to factors such as component aging, thermal variations and environmental changes. It can also track vibrations in the SMPCs caused by disturbances such as satellite maneuvers, space radiation pressure and gravity gradient torques. Therefore, the novel algorithm designed in this study demonstrates excellent adaptability and efficiency in complex dynamic environments, making it highly suitable for AVC of SMPCs in space environments.

4. Investigation of the proposed control algorithm in SMPCs

In this section, we investigate the proposed control algorithm applied to SMPCs through comprehensive experiments and analyses. Firstly, we prepare SMPC specimens and establish boundary conditions, showcasing their deformation capabilities and detailing the material composition and manufacturing process. Secondly, we analyze the dynamic characteristics of SMPCs, utilizing experimental systems to measure damping ratios and frequency responses, demonstrating the effects of fiber volume fraction on mechanical properties. Finally, we conduct AVC experiments under multilinear spectrum conditions, comparing the effectiveness of the control algorithm on SMPCs in both original and bent shapes. This progression from preparation to dynamic analysis and control experimentation illustrates the algorithm's adaptability and effectiveness.

4.1. Preparation and boundary conditions of SMPC specimens

SMPCs serve as intelligent materials capable of bidirectional deformation, with their operational process illustrated as in Fig. 12. The thermal deformation process is divided into program and recovery steps. During the program step, as shown in Fig. 12 (a), SMPCs are heated above the transition temperature (*Ttrans*), where the elastic modulus is relatively low, allowing the material to deform from its original shape to a bent shape under the application of an external force. By maintaining this external force and subsequently cooling below *Ttrans*, the SMPCs gradually increase in stiffness. Upon removal of the external force, most of the pre-strain is stored in the form of stored strain within the SMPCs, allowing them to retain a bent shape, thus completing the shape programming from $\theta = 0°$ to $\theta = 180°$. During the recovery step, as shown in Fig. 12 (b), with the SMPCs unloaded and heated above the transition temperature, the stored strain energy is released, enabling the material to automatically revert to its original shape, i.e., $\theta = 0°$. Fig. 12 (c) illustrates the dynamic deployment process of a single-layer carbon fiber fabric reinforced SMPC.

This manuscript selects two shapes of SMPCs as models for vibration control: the original shape and the bent shape, representing the two typical operational states of SMPCs in practical applications.

The SMP material used in this study is an epoxy-based shape memory resin developed by the Jinsong Leng's research group, with a glass transition temperature of 100 °C [60]. The carbon fiber (T300-3 K, plain weave) reinforced shape memory composites were manufactured using the Vacuum-Assisted Resin Transfer Molding (VARTM) process. The carbon fiber fabrics were stacked in one, two, three, four and five layers

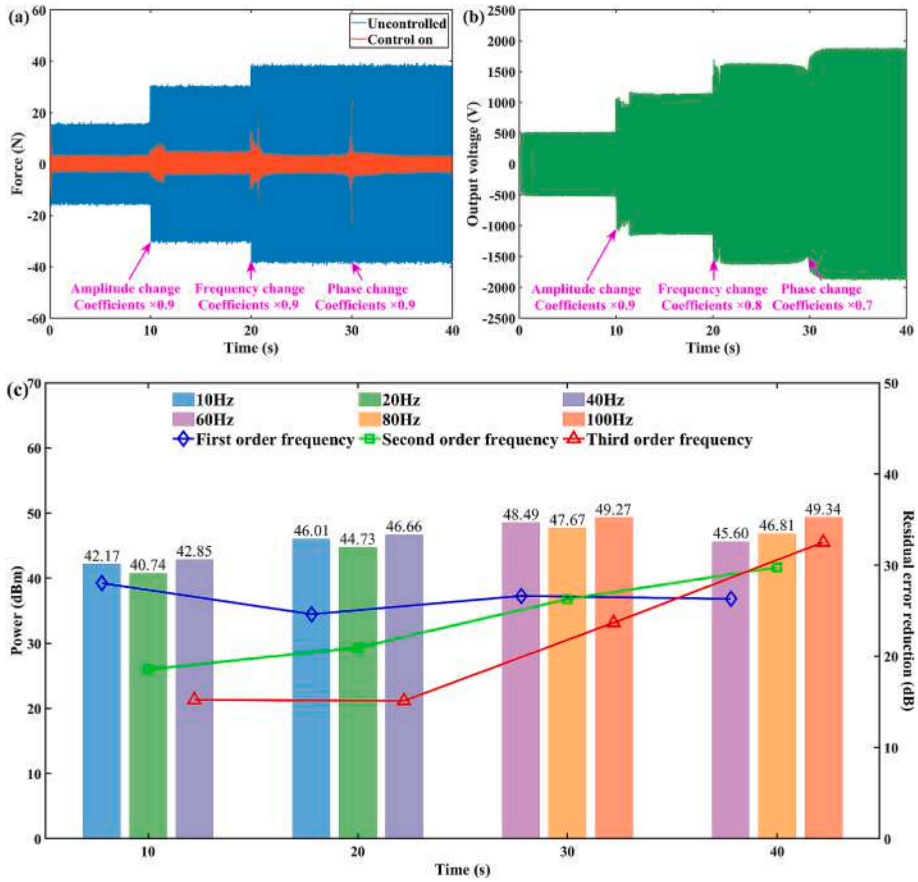

Fig. 11. Adaptability examination results of the proposed controller with the amplitude, frequency and phase change simultaneously with secondary paths: (a) force response, (b) output voltage of the controller, (c) line spectral power and its residual error reduction change.

on five different Teflon molds. The height of the VARTM molds was set at 3 mm. A vacuum was maintained inside the molds while the mixture of SMP and curing agent was injected into the fabric layers. The molds were then hot-pressed at 100 °C for one hour. After demolding, specimens of CF-SMPC with varying fiber volume fractions were cut from the prepared composites, each with dimensions of 220 mm x 20 mm x 3 mm.

The variable v_f represents the fiber volume fraction in SMPCs. Apart from this, all specimens were identically configured to ensure consistent experimental conditions. The boundary conditions are set as shown in Fig. 13. The clamped end is 20 mm long. The exciter applies an active force perpendicular to the specimen, with the excitation point 10 mm from the fixed end. The MFC is adhered to the AVC zone from 40 mm to 80 mm. An electric heating film is affixed to the thermal deformation area from 100 mm to 140 mm. When the SMPCs are in their original shape, the vibration displacement monitoring point is located 10 mm from the free end. When the electric heating film is powered and the heating temperature is set to 100 °C, the SMPCs adopt a bent shape, and the vibration displacement monitoring point moves to 70 mm from the free end.

4.2. Dynamic characteristic analysis

Fig. 14 (a) displays the AVC experimental system, which comprises the experimental object, temperature control system, excitation system and active control system. The experimental object consists of SMPC specimens with varying carbon fiber volume contents. By adjusting the temperature settings of the temperature control device and toggling the electrical heating film's circuit state, the SMPCs can be transitioned between two distinct shapes, such as from the original shape shown in Fig. 14 (b) to the bent shape shown in Fig. 14 (c). The external excitation system stimulates the experimental object. The active control system is composed of three main components: the signal acquisition system, computer processing system and signal output system. The signal acquisition system includes force sensors mounted on the exciter's top rod and laser displacement sensors, which measure the output force of the excitation device and the displacement at the free end of the SMPCs, respectively. These measurements serve as the basis for control strategies and can be used to evaluate the effectiveness of the proposed vibration control methods.

The root of the SMPCs was struck with a force hammer, and the displacement response at the free end was recorded. The damping of each SMPC specimen was calculated using the free decay oscillation method for the vibration attenuation waveform, as shown in Fig. 15. With the increase in fiber volume fraction (v_f), the damping ratio of the specimens gradually decreased. The damping ratio of the v_{f1} specimen was significantly higher than that of the other specimens because the carbon fiber volume fraction was relatively low, resulting in the matrix being the major component. Consequently, the damping ratio of the v_{f1} specimen was close to that of the epoxy resin matrix. The damping ratios of specimens v_{f3} and v_{f4} are closely matched, and the damping of these two composite materials aligns with the damping of the epoxy resin matrix. The damping ratio of specimen v_{f5} is the lowest, recorded at

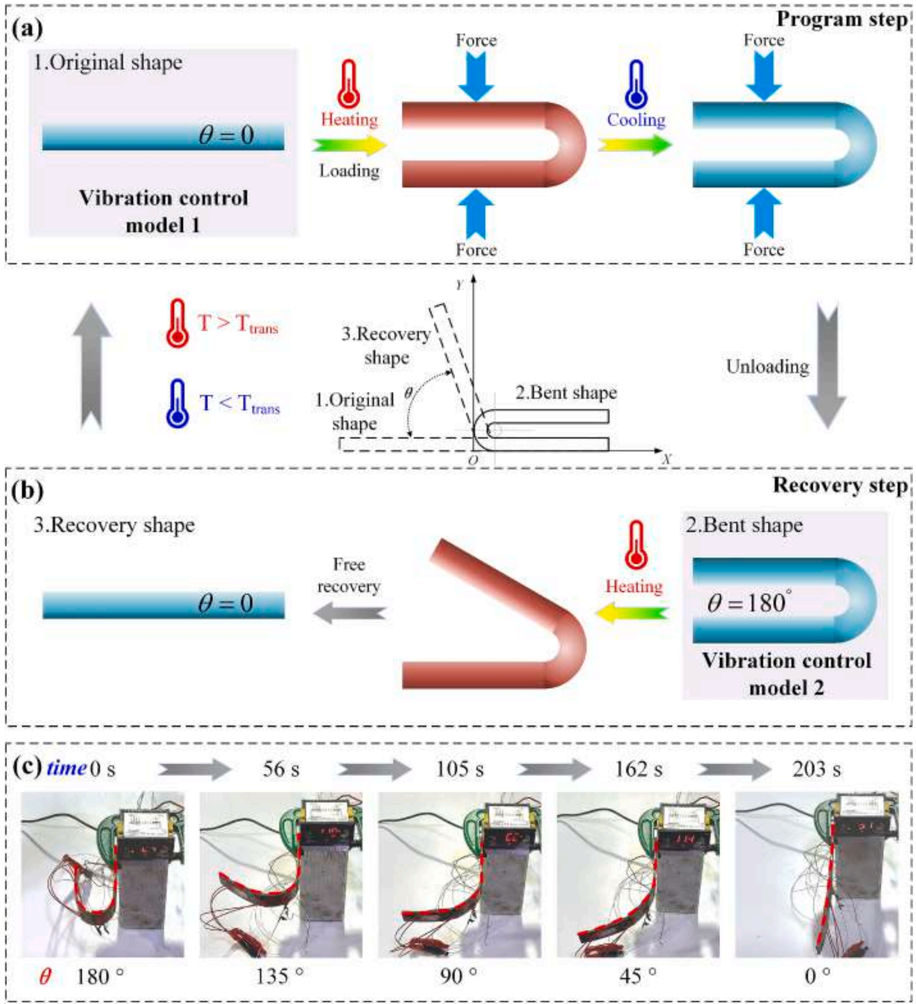

Fig. 12. Schematic of thermomechanical deformation process of SMPCs: (a) program step, (b) recovery step, (c) recovery process of single-layer carbon fiber fabric reinforced SMPC.

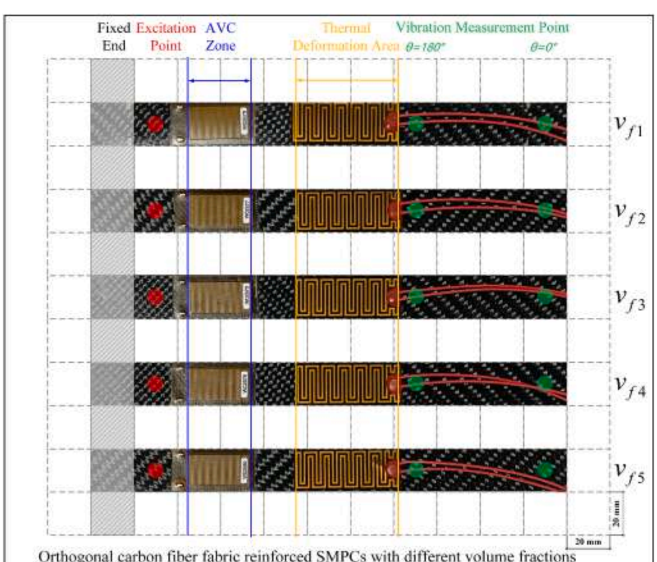

Fig. 13. The boundary settings for SMPCs reinforced with carbon fiber fabrics of different volume fractions.

0.0136, where the five layers of carbon fiber fabric result in the slowest attenuation of vibrational energy in the SMPCs.

The basic mechanical parameters of the carbon fiber layers and the pure epoxy matrix layers at room temperature are shown in Table 3. Based on the parameters in the table, the FRF of the specimen was calculated, as shown in Fig. 16 (a). The x-coordinate corresponding to the peak of the FRF indicates the natural frequency of the SMPC specimen. The results indicate that as the fiber volume fraction increases, the first three natural frequencies of the specimen also increase. An adaptive control strategy was applied for the vibration control of the specimen, and the impact of the controller's introduction on the frequency response of the SMPCs was theoretically analyzed. Since the adaptive control strategy analyzes the time-domain signal, a simplified analysis was performed, considering the effect of the system output at any given time on the specimen's FRF, as shown in Fig. 16 (b). After applying the adaptive control algorithm to the vibration control of the SMPCs, the overall magnitude of the frequency response decreased, and the FRF curve shifted downward. The decrease in the peak value corresponding to the natural frequencies before and after control reduced as the fiber volume content increased, with each specimen's natural frequency increasing and the FRF curve shifting to the right. This indicates that the introduction of the AVC strategy increased both the equivalent mass and equivalent damping of the SMPCs.

Considering the absence of transverse and plane loads, the equation of free vibration for the plate is:

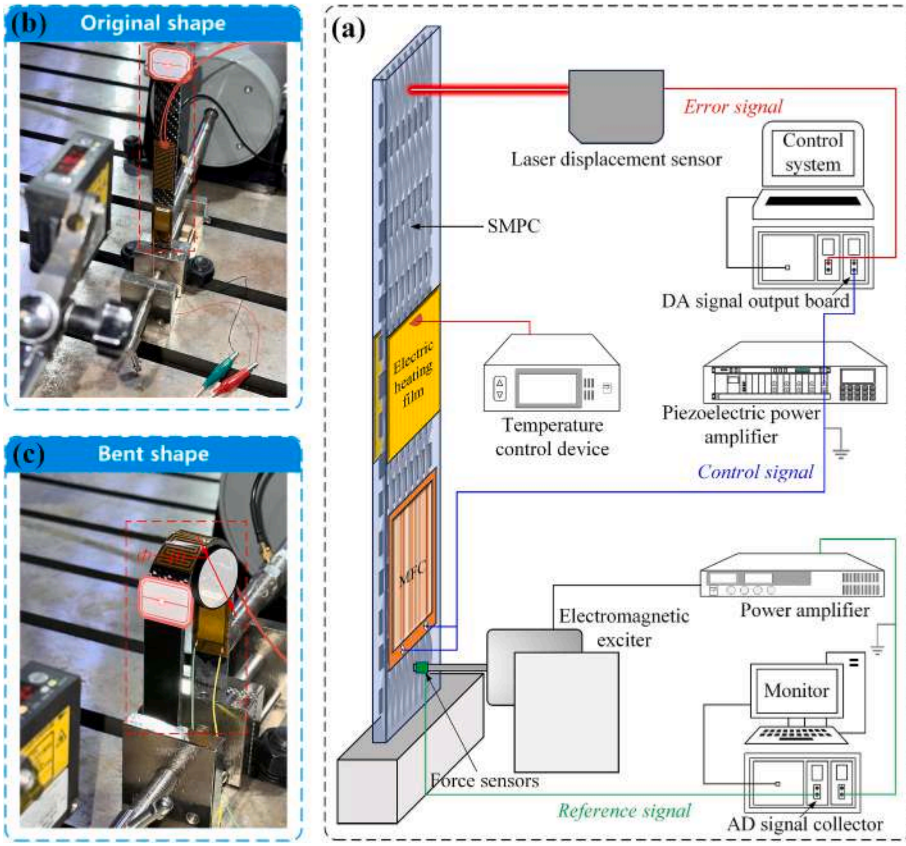

Fig. 14. AVC experimental system: (a) overall composition of the system, (b) AVC of SMPCs in original shape, (c) AVC of SMPCs in bent shape.

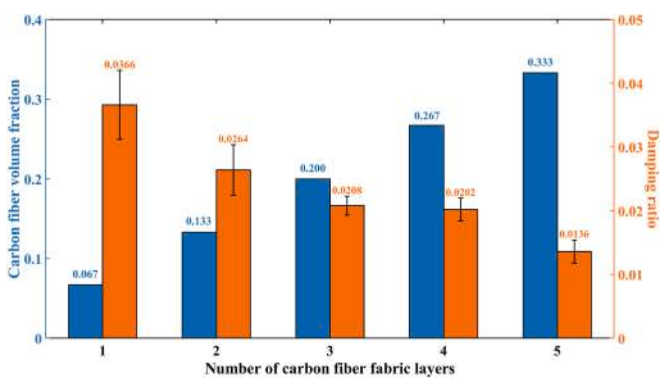

Fig. 15. Damping ratio and carbon fiber volume fraction for the SMPC specimens.

$$
\begin{aligned}
&D_{11}\delta w_{,xxxx} + 2(D_{12} + 2D_{66})\delta w_{,xxyy} + D_{22}\delta w_{,yyyy} \\
&\quad + 4D_{16}\delta w_{,xxxy} + 4D_{26}\delta w_{,xyyy} + \rho h \delta w_{,tt} = 0
\end{aligned} \tag{16}
$$

When both the reinforcement phase and the matrix phase are isotropic materials, then $D_{11} = D_{22} = (D_{12} + 2D_{66}) = D = \frac{Eh^3}{12(1-\nu^2)}, D_{16} = D_{26} = 0$. The differential equation governing the free vibration of the plate can be written as:

$$
D\nabla^4 w(x,y,t) + \rho h \frac{\delta^2 w(x,y,t)}{\delta t^2} = 0 \tag{17}
$$

where $w(x,y,t)$ is the deflection function of the plate, representing the displacement. ∇^4 is the biharmonic operator. ρ is the density of the material. h is the thickness of the plate.

Due to the capability of the bi-directional beam function method to accurately represent the deflection modes of composite thin plates and achieve sufficient precision with a finite number of terms, this method is adopted to analyze and obtain the natural frequencies and mode shapes. For harmonic free vibration, the deflection can be expressed as a superposition of an infinite number of mode functions:

$$
w(x,y,t) = \sum_{m=1}^{\infty}\sum_{n=1}^{\infty}\Phi_{mn}(x,y)\eta_{mn}e^{i\omega t} \tag{18}
$$

where η_{mn} is the modal amplitude of the (m,n)-th mode. $\Phi_{mn}(x,y)$ are the mode functions.

By substituting the expression for $w(x,y,t)$ from Eq. (18) into the governing differential Eq. (17), we obtain:

$$
D\nabla^4\Phi_{mn}(x,y) - \rho h \omega_{mn}^2 \Phi_{mn}(x,y) = 0 \tag{19}
$$

Here, ω_{mn} is the natural frequency of the (m,n)-th mode. The mode shapes of a plate can be conveniently represented as the product of two independent beam functions, one for each principal direction of the plate.

$$
\Phi_{mn}(x,y) = X_m(x)\cdot Y_n(y) \tag{20}
$$

Specifically, the m-th mode shape function along the x-direction can be represented by the fixed-free beam function:

Table 3
Material parameters for the SMPCs.

Parameters	Density (kg/m^3)	Tensile modulus (GPa)	Poisson's ratio	Shear modulus (GPa)
Epoxy resin matrix	1500	2.0	0.38	0.7
Carbon fiber fabrics	1000	39.9	0.20	1.5

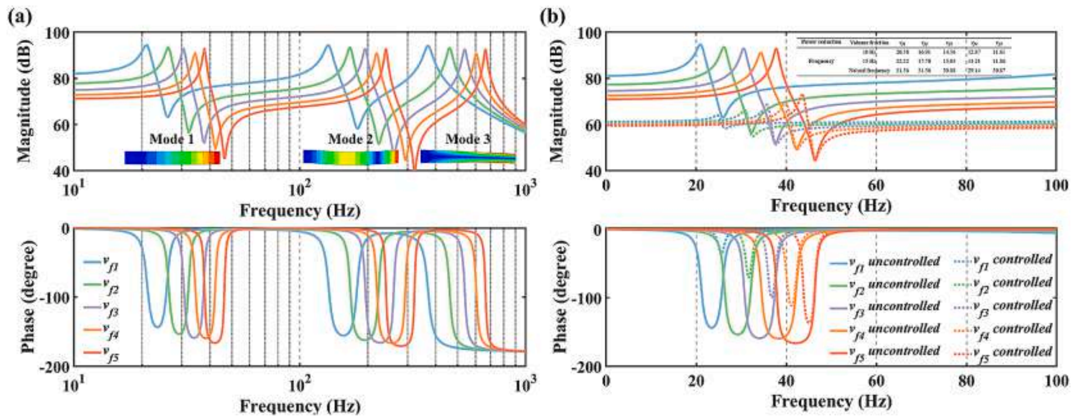

Fig. 16. Dynamic characteristics of the original SMPC specimens: (a) frequency response function, (b) frequency domain response comparison with adaptive control module.

$$X_m(x) = \cosh\left(\frac{\lambda_m x}{L_x}\right) - \cos\left(\frac{\lambda_m x}{L_x}\right) - \sigma_m\left[\sinh\left(\frac{\lambda_m x}{L_x}\right) - \sin\left(\frac{\lambda_m x}{L_x}\right)\right] \tag{21}$$

where λ is the root of the equation $\cosh(\lambda)\cos(\lambda) = 1$. The solution for λ_m and σ_m are as follws:

$$\lambda_1 = 1.875, \lambda_2 = 4.694, \lambda_3 = 7.854, \cdots, \lambda_m = \frac{2m-1}{2}\pi$$

$$\sigma_1 = 0.7341, \sigma_2 = 1.0185, \sigma_3 = 0.9992, \cdots, \sigma_m = \frac{\cosh(\lambda_m) + \cos(\lambda_m)}{\sinh(\lambda_m) + \sin(\lambda_m)}$$

While the n-th mode shape function along the y-direction can be represented by the free-free beam function $Y_n(n)$:

$$\begin{cases} Y_1(y) = 1 \\ Y_2(y) = 1 - \dfrac{2y}{L_y} \\ Y_n(y) = \cosh\left(\dfrac{\lambda_n y}{L_y}\right) + \cos\left(\dfrac{\lambda_n y}{L_y}\right) - \sigma_n\left[\sinh\left(\dfrac{\lambda_n y}{L_y}\right) + \sin\left(\dfrac{\lambda_n y}{L_y}\right)\right] (n \geqslant 3) \end{cases} \tag{22}$$

The natural frequency can be found:

$$\omega_{mn} = \sqrt{\frac{D}{\rho h}} \cdot \sqrt{\frac{I_1 I_2 + 2 I_3 I_4 + I_5 I_6}{I_2 I_6}} \tag{23}$$

Where

$$I_1 = \int_0^{Lx} \frac{\partial^4 X_m(x)}{\partial x^4} X_m(x) dx, I_2 = \int_0^{Ly} [Y_n(y)]^2 dy$$

$$I_3 = \int_0^{Lx} \frac{\partial^2 X_m(x)}{\partial x I^2} X_m(x) dx, I_4 = \int_0^{Ly} \frac{\partial^2 Y_n(y)}{\partial y^2} Y_n(y) dy$$

$$I_5 = \int_0^{Ly} \frac{\partial^4 Y_n(y)}{\partial y^4} Y_n(y) dy, I_6 = \int_0^{Lx} [X_m(x)]^2 dx$$

A frequency sweep experiment was conducted on the SMPC specimen to verify the correctness of the theoretical predictions regarding its dynamic characteristics. Based on the boundary conditions, the displacement of the specimen's free end and the input force from the exciter were collected. After processing the data in the frequency domain, the FRF for different fiber volume fractions were obtained, as shown in Fig. 17 (a). The curve variation patterns were similar to the theoretical predictions, with the specimen's natural frequencies increasing as the fiber volume fraction increased. The first-order natural frequency is listed in Table 4. The results indicate that the theoretical calculations at low frequencies (from Eq. (23)) align well with the experimental natural frequency results. As seen in the figure, the FRF of the specimen in the 0–500 Hz range includes not only the first three

Table 4
The first order natural frequency of the SMPC specimen.

Parameters	v_{f1}	v_{f2}	v_{f3}	v_{f4}	v_{f5}
Theoretical calculation results (Hz)	21.12	26.13	30.57	34.46	37.80
Experimental frequency sweep (Hz)	20.02	24.03	30.69	34.53	37.45

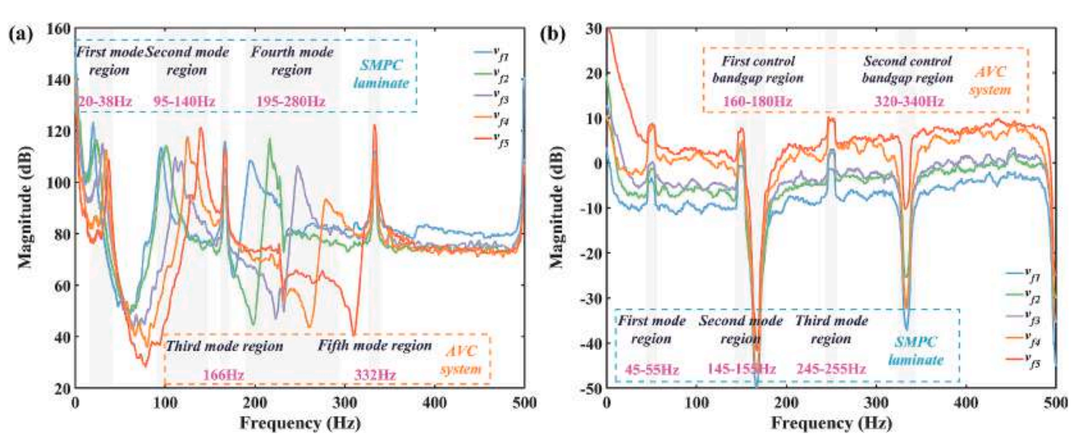

Fig. 17. Experimental frequency response curves of the original SMPC specimens: (a) primary force at the excitation point as the input signal, (b) control force in the AVC zone as the input signal.

modes of the SMPC laminate but also two resonances generated at 166 Hz and 332 Hz due to the introduction of the active control system. When conducting the frequency sweep with MFC, the displacement of the specimen's free end and the input voltage of the MFC were collected, and the FRF curve of the SMPCs under the control force was plotted, as shown in Fig. 17 (b). The curve shows distinct response protrusions in the frequency bands of 45–55 Hz, 145–155 Hz and 245–255 Hz, with two control forbidden zones near 166 Hz and 332 Hz, which correspond to the two resonance zones brought by the control system as shown in Fig. 17 (a). The frequency response of the MFC control force in the 0–500 Hz range increased overall with the increase in fiber volume fraction. The results indicate that as the stiffness of the SMPCs increases, the control performance of the MFC improves.

4.3. AVC experiment under multilinear spectrum based on MFC

4.3.1. Vibration control model 1: SMPCs of the original shape

The experiment of multilinear spectrum vibration control on the original shape of SMPCs using MFC was conducted, with each specimen selecting a signal composed of three harmonic waves superimposed as the vibration input, respectively at 10 Hz, 15 Hz and the first-order natural frequency. The results of the multilinear spectrum vibration

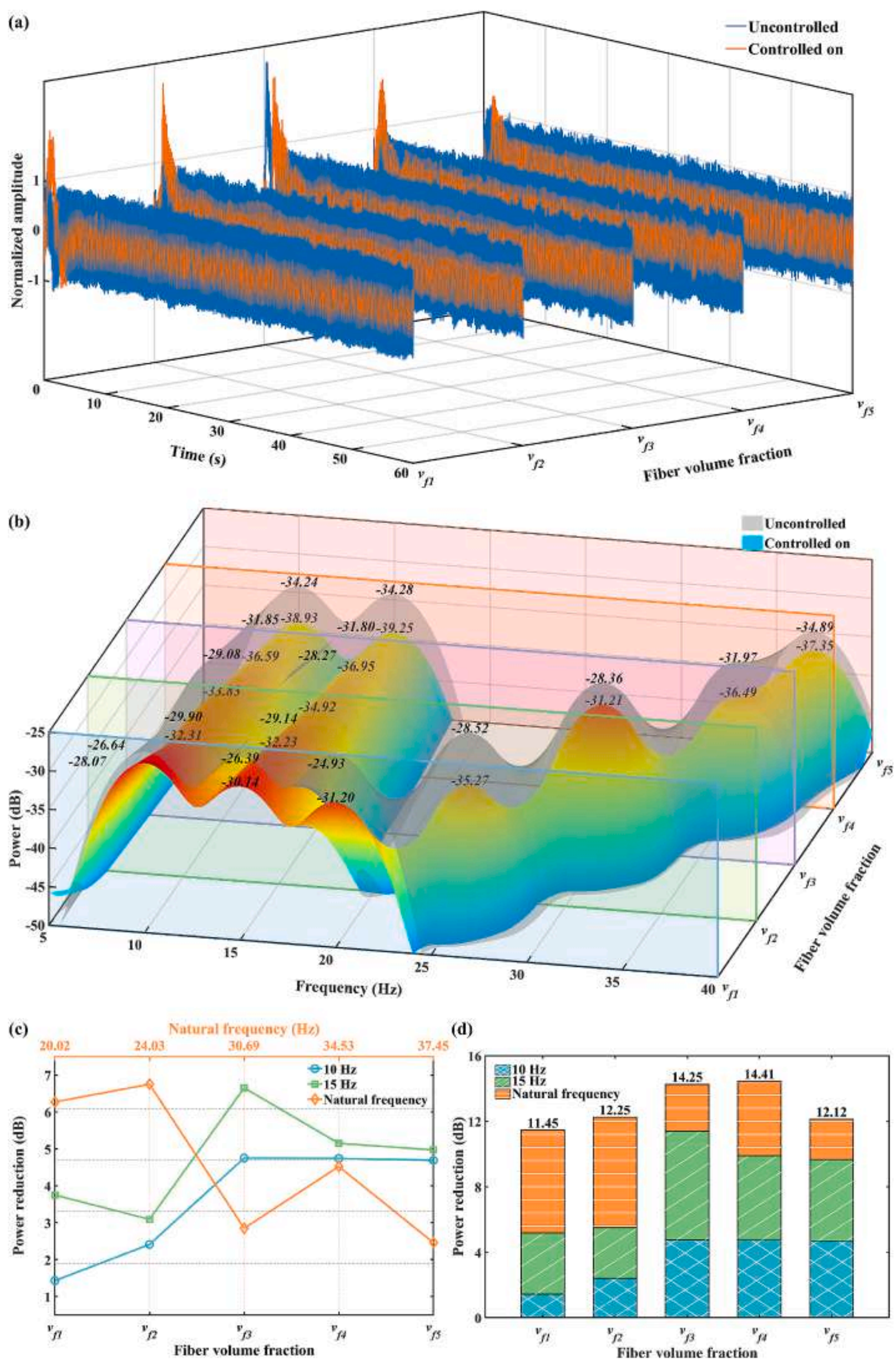

Fig. 18. The experimental results for the original SMPCs: (a) time-domain displacement response from 0-60 s, (b) frequency-domain displacement power response from 30-60 s, (c) power of each linear spectrum varies with fiber volume fraction, (d) power of multilinear spectrum varies with fiber volume fraction, (e) power of multilinear spectrum in different observation periods, (f) optimal and sub-optimal fiber volume fraction variation rules for vibration control.

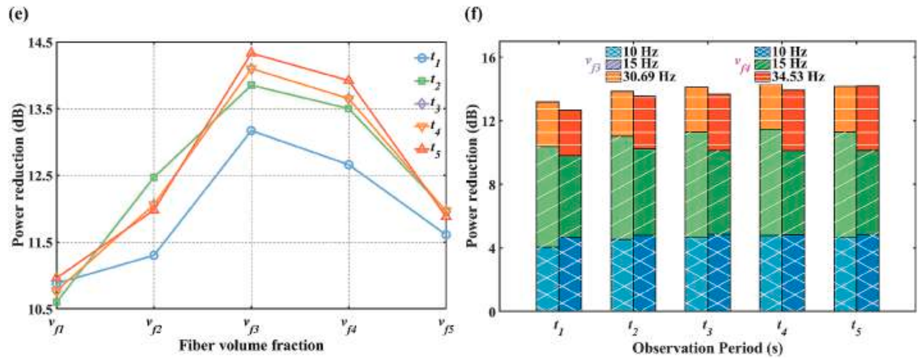

Fig. 18. (*continued*).

control experiment are shown in Fig. 18. Fig. 18 (a) shows the time-domain control effects for different fiber volume fractions, with each specimen achieving vibration convergence within a few seconds. Once the system stabilizes, the vibration suppression rates for the SMPC specimens with the five fiber volume fractions (calculated by the RMS of amplitude from 10 to 60 s) are 50.12 %, 47.25 %, 45.23 %, 54.79 % and 48.25 %, respectively. During the initial phase, inherent response times and dynamic delays in the sensors, actuators and signal processing units can lead to transient effects such as current fluctuations or mechanical responses. These accumulated delays cause a lag in system response, resulting in a temporary mismatch between the output control signal and the actual vibration, which in turn leads to overshoot, manifested as an initial surge. Overall, this overshoot is caused by the switching states of the hardware system, which to some extent, validates the stability of the proposed algorithm.

The power spectrum before and after vibration control are shown in Fig. 18 (b). The upper surface is composed of the power of the uncontrolled linear spectrum for different fiber volume fractions, and the power surface after control is all located below, indicating that the proposed algorithm has a good suppression effect on the vibration power of the multilinear spectrum and its nearby frequency domain. Fig. 18 (c) and (d) show the variation patterns of the single power control and overall power control of the three line spectrum with the fiber volume fraction, respectively. The control effect of the first line spectrum improves with the increase of the fiber volume fraction, with a more obvious trend for the first three volume fraction specimens, while there is almost no change for the last two volume fraction specimens. The control effects at the second line spectrum and the natural frequency fluctuate up and down with the increase of the fiber volume fraction, and the fluctuation directions of the power control quantities at the two frequencies are opposite. Fig. 18 (c) indicates that as the fiber volume content and natural frequency of the specimens increase, the control effect of the linear spectrum at the lowest frequency becomes better, and the energy of the control signal flows back and forth between the second and third frequencies. Fig. 18 (d) shows that the reduction amount of the overall power of the linear spectrum first increases and then decreases, with the best suppression effect on the multilinear spectral power for the v_{f3} and v_{f4} specimens. Combining the conclusions drawn from Fig. 16 (b) and Fig. 17 (b), this experimental pattern is reasonable.

Considering the impact of different time scales on the reduction of vibration linear spectral power, the experimental results are shown in Fig. 18 (e) and (f). t_1, t_2, t_3, t_4 and t_5 represent 10–60 s, 20–60 s, 30–60 s, 40–60 s and 50–60 s, respectively. The experimental results show that as the time scale shrinks, the reduction of power for each linear spectral and the overall linear spectral power increases, that is, the control effect of the AVC system becomes better over time, consistent with the simulation trend.

4.3.2. *Vibration control model 2: SMPCs of the bent shape*

An experimental study on the AVC of bent SMPCs was conducted. The electric heating films were used to heat the SMPC specimens, bending them to 180° as shown in Fig. 14 (c). The frequency sweep for the bent v_{f1}, v_{f3} and v_{f5} specimens was performed using both an exciter and MFC, with the results shown in Fig. 19 (a) and (b). From Fig. 19 (a), it is observed that the first-order natural frequencies of the bent SMPC specimens increased to 56.15 Hz, 62.01 Hz and 67.82 Hz, respectively. The deformation process of the SMPCs led to an increase in the natural frequencies by 35.03 Hz, 31.32 Hz, and 30.37 Hz, respectively. Fig. 19 (b) shows that after deformation, the MFC caused a complete transformation of the resonance regions and forbidden bands of the specimens. As indicated by Fig. 19 (b), after the deformation of the SMPCs, there is a complete transformation in the resonance regions and forbidden bands of the specimens when compared to the situation depicted in Fig. 17 (b). This transformation suggests that the deformation of the SMPCs has significantly altered the dynamic behavior of the specimens, particularly in terms of how the MFC interacts with the

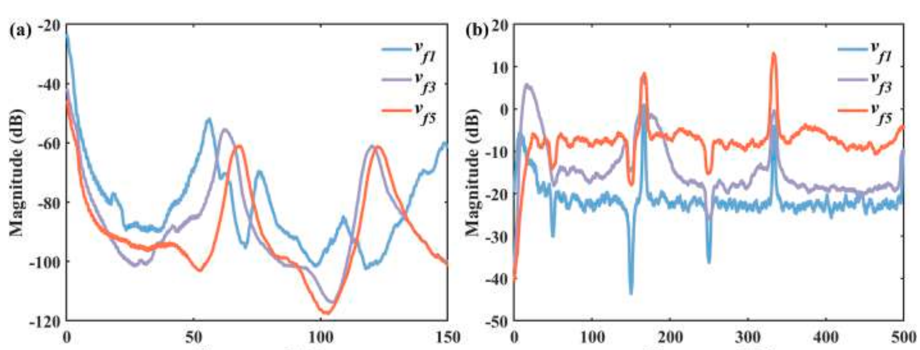

Fig. 19. Experimental frequency response curves of the bent SMPC specimens: (a) primary force at the excitation point as the input signal, (b) control force in the AVC zone as the input signal.

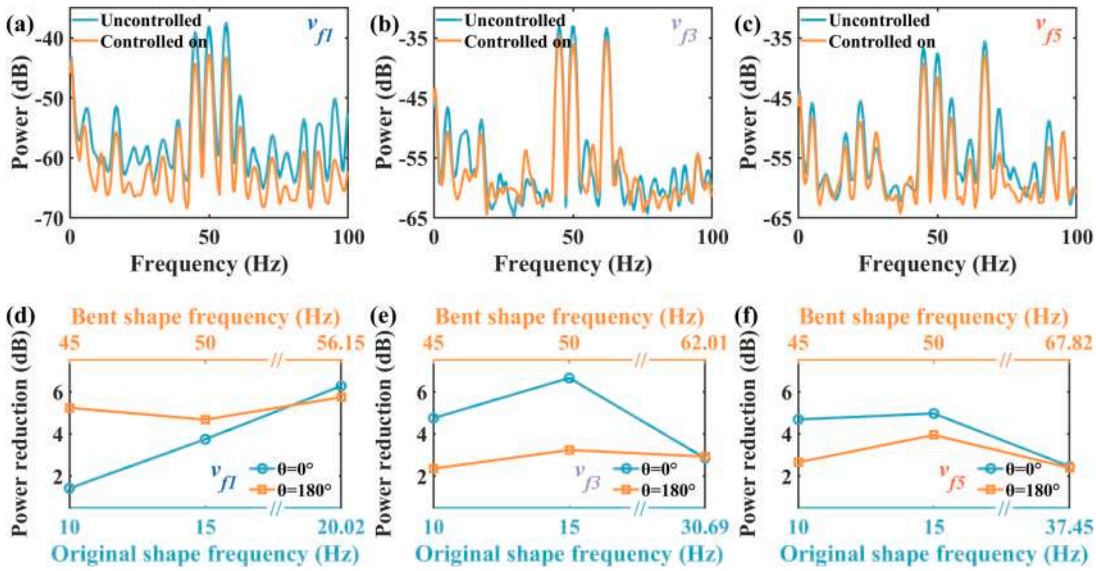

Fig. 20. The experimental results for the bent SMPCs: the power spectrum comparison before and after vibration control for (a), (b) and (c), corresponding to fiber volume fractions v_{f1}, v_{f3} and v_{f5}. The comparison of multilinear spectral power attenuation for (d), (e) and (f), representing SMPCs with different fiber volume fractions, under their original shapes and bent shapes.

specimens' vibration characteristics. This change could be due to the altered structural properties of the SMPCs post-deformation, such as changes in stiffness, mass distribution or boundary conditions, which in turn affect the frequency response.

Based on the proposed adaptive algorithm, an active vibration control experiment was conducted on the bent SMPCs using multilinear spectrum excitation. The vibration excitation signals were set at 45 Hz, 50 Hz and the first-order natural frequency of the bent specimens. The experimental results are shown in Fig. 20. Fig. 20 (a), (b) and (c) show the power spectrum curves of the three specimens before and after control. It can be seen that the proposed control strategy has a significant suppression effect on the power of the multilinear spectrum, and it also has some effect at other frequencies. Fig. 20 (d), (e) and (f) compare the line spectral power suppression effects of the same specimens in their original and bent shapes. The results indicate that the trend of line spectrum power reduction with frequency is consistent in both states. Except for the v_{f1} specimen, the vibration control effect in the bent shape is not as effective as in the original shape, particularly at the lower frequencies of the first two excitation signals. The comparison of the FRF in Fig. 19 (b) and Fig. 17 (b) suggests that the control effectiveness of the MFC is weaker for the bent shape compared to the original shape of the SMPCs. This could be attributed to several factors:

(1) Material property changes: The deformation of the SMPCs may have altered their material properties, such as stiffness and damping, which could affect the coupling efficiency between the MFC and the SMPCs.
(2) Boundary conditions: The bending of the SMPCs may have changed the boundary conditions, leading to a different mode shape and natural frequencies, which could reduce the effectiveness of the MFC.
(3) Strain distribution and actuation efficiency: The strain distribution within the SMPCs after bending might be non-uniform, which could limit the ability of the MFC to effectively apply

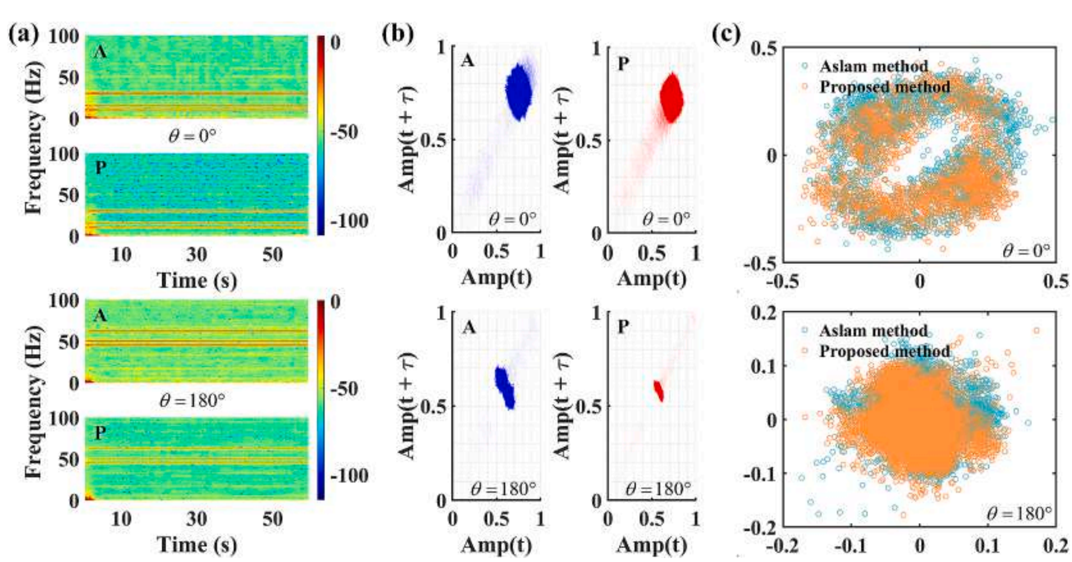

Fig. 21. Comparison of experimental results between the proposed method (P) and the traditional method (A): (a) time–frequency diagram, (b) phase trajectory diagram, and (c) Poincaré section of vibration signal.

control forces across the entire structure. Besides, the efficiency of the MFC actuation might be reduced in the bent configuration due to changes in the stress and strain fields, which could diminish the control authority.

In the experiments, the Aslam method, which performed best among traditional algorithms, was selected for vibration control experiments on the v_{f3} specimen under multiple configurations. The experimental results, as shown in Fig. 21, compare the proposed method with the traditional one in terms of convergence speed, model accuracy, stability, etc. From Fig. 21 (a), it can be seen that both methods can clearly distinguish the frequency of the vibration signal within the 0–60 s range. The colors in the figure represent the power at corresponding frequencies. It is evident that for both the original and bent configurations of the SMPCs, the proposed method converges more quickly in the initial few seconds, with lower power in the line spectrum, manifested as lighter stripes closer to the initial moment. Additionally, it is observed that the higher the frequency of the line spectrum, the better the convergence speed and suppression effect. Furthermore, for frequency bands outside the controlled line spectrum, the overall lighter color of the power indicates that the proposed method also achieves better control effects for broadband random vibrations at non-controlled frequencies. Fig. 21 (b) presents the phase portrait diagram of the vibration signal. It can be seen that the signal trajectory controlled by the Aslam method is sparse, whereas the trajectory controlled by the proposed method is dense, indicating greater stability of the proposed method. In contrast, the traditional method's controller exhibits more significant dynamic characteristics and nonlinear behavior. Besides, the phase trajectory of the bent configuration is noticeably smaller than that of the original configuration. This is because, in the deployed state, the free end of the SMPC is further from the fixed end, resulting in the vibration signal containing more nonlinear and random vibrations. Fig. 21 (c) shows the Poincaré section at a height of 0 in the phase portrait diagram. It can be observed that whether the system vibration is in a periodic or chaotic state, both methods show consistency. However, for periodic motion ($\theta = 0^\circ$), the proposed method demonstrates better linear behavior. In the case of chaotic states ($\theta = 180^\circ$), the proposed method can more quickly identify the features of the system's complex dynamics.

5. Conclusions

In this manuscript, a new scheme to control vibrations in a system was established by utilizing enhanced online secondary path modelling. The method dynamically adjusts the step size based on the status of the AVC system, and the method was simulated and compared with existing methods. The results demonstrate that our proposed method enhances the convergence speed and modelling accuracy without compromising the vibration control efficacy. Additionally, its computational complexity remains on par with that of previous methods. According to numerical simulations, the proposed controller demonstrates high adaptability in handling various external excitations and secondary paths. It effectively mitigates structural vibration responses caused by sudden changes in drive performance or input signals through the adjustment of control voltage. The investigation into the AVC of SMPCs in both their original and bent configurations has provided valuable insights into their dynamic behavior and control performance. Results indicate that the proposed adaptive control strategy effectively reduced vibrations in both configurations, demonstrating the algorithm's adaptability and potential to enhance control effectiveness. This research underscores the potential of integrating adaptive control algorithms with intelligent materials like SMPCs, paving the way for broader applications in dynamic environments and advanced engineering solutions.

With the advancement of deep space exploration, space stations and high-precision satellites, the structure of spacecraft has become increasingly complex. Due to the constraints of launch costs and carrying capacity, spacecraft structures have also become more flexible. Consequently, multilinear spectrum vibration control technology with online identification capability has become one of the key technologies for spacecraft. Multiharmonic vibration can significantly affect the performance of spacecraft during their operational lifespan, particularly impacting flexible structures such as onboard antennas, flexible trusses and solar sails. This study provides a feasible solution for the vibration control of these deployable cantilever structures in space environments. However, the challenges of lightweight, miniaturized and highly integrated AVC systems remain to be addressed. Future work needs to further optimize the control system and validate the feasibility of the proposed technologies in space environments. In addition, the weight update of the adaptive algorithm depends on the controller step size. If the step size is too small, the convergence speed will be slow. If it is too large, it may lead to system instability. Before applying the algorithm from this study in engineering practice, it is necessary to pre-set the step size reasonably for specific environments. In the future, leveraging the powerful capabilities of artificial intelligence and large models can transform the adjustment of the controller step size from a static, experience-driven mode to a dynamic, adaptive intelligent optimization mode, thereby enhancing the applicability of the system in engineering scenarios.

CRediT authorship contribution statement

Weikai Shi: Writing – review & editing, Writing – original draft, Visualization, Investigation, Formal analysis, Conceptualization. **Xudong Zhang:** Writing – review & editing, Visualization, Data curation. **Peilei Xu:** Validation, Methodology, Investigation, Data curation. **Jianlong Gao:** Writing – review & editing, Visualization, Data curation. **Pengxiang Zhao:** Writing – review & editing, Visualization, Data curation. **Yaxiang Sun:** Writing – review & editing, Visualization, Data curation. **Xin Lan:** Writing – review & editing, Validation, Methodology, Data curation. **Jinsong Leng:** Writing – review & editing, Supervision, Investigation. **Yanju Liu:** Writing – review & editing, Investigation, Conceptualization.

Declaration of competing interest

The authors declare that they have no known competing financial interests or personal relationships that could have appeared to influence the work reported in this paper.

Acknowledgements

The authors wish to acknowledge the support given by the National Natural Science Foundation of China (Grant no. 12272113).

Data availability

Data will be made available on request.

References

[1] Ma L, Zhu Y, Wang M, Yang X, Song G, Huang Y. Enhancing interfacial strength of epoxy resin composites via evolving hyperbranched amino-terminated POSS on carbon fiber surface. Compos Sci Technol 2019;170:148–56.
[2] Randall JD, Eyckens DJ, Servinis L, Stojcevski F, O'Dell LA, Gengenbach TR, et al. Designing carbon fiber composite interfaces using a 'graft-to' approach: Surface grafting density versus interphase penetration. Carbon 2019;146:88–96.
[3] Leng J, Lan X, Liu Y, Du S. Electroactive thermoset shape memory polymer nanocomposite filled with nanocarbon powders. Smart Mater Struct 2009;18.
[4] Lan X, Liu Y, Lv H, Wang X, Leng J, Du S. Fiber reinforced shape-memory polymer composite and its application in a deployable hinge. Smart Mater Struct 2009;18.
[5] Liu Y, Lv H, Lan X, Leng J, Du S. Review of electro-active shape-memory polymer composite. Compos Sci Technol 2009;69:2064–8.
[6] Leng J, Lan X, Liu Y, Du S. Shape-memory polymers and their composites: stimulus methods and applications. Prog Mater Sci 2011;56:1077–135.

[7] Tomizuka M, Liu Y, Wang X, Lan X, Lv H, Leng J. Shape memory polymer composite and its application in deployable hinge for space structure. Sensors Smart Struct Technol Civil Mech Aeros Syst 2008.
[8] Liu T, Liu L, Yu M, Li Q, Zeng C, Lan X, et al. Integrative hinge based on shape memory polymer composites: material, design, properties and application. Compos Struct 2018;206:164–76.
[9] Zhang D, Liu L, Xu P, Zhao Y, Li Q, Lan X, et al. World's first application of a self-deployable mechanism based on shape memory polymer composites in Mars explorations: ground-based validation and on-Mars qualification. Smart Mater Struct 2022;31.
[10] Xu P, Lan X, Zeng C, Zhang X, Liu Y, Leng J. Dynamic characteristics and active vibration control effect for shape memory polymer composites. Compos Struct 2023;322.
[11] Qi R, Wang L, Zhou X, Xue J, Jin J, Yuan L, et al. Embedded piezoelectric actuation method for enhanced solar wings vibration control. Int J Mech Sci 2024;274.
[12] Gao Y, Wang L. Broad bandgap active metamaterials with optimal time-delayed control. Int J Mech Sci 2023;254.
[13] Xu Y, Yang T, Fuller CR, Sun Y, Liu Z. A theoretical analysis on the active structural acoustical control of a vibration isolation system with a coupled plate-shell foundation. Int J Mech Sci 2020;170.
[14] Chang Y, Zhou J, Wang K, Xu D. Theoretical and experimental investigations on semi-active quasi-zero-stiffness dynamic vibration absorber. Int J Mech Sci 2022;214.
[15] Loewy RG. Helicopter vibrations: a technological perspective. J Am Helicopter Soc 1984;29:4–30.
[16] Song ZG, Zhang LW, Liew KM. Active vibration control of CNT reinforced functionally graded plates based on a higher-order shear deformation theory. Int J Mech Sci 2016;105:90–101.
[17] He H, Li Y, Jiang JZ, Burrow S, Neild S, Conn A. Using an inerter to enhance an active-passive-combined vehicle suspension system. Int J Mech Sci 2021;204.
[18] Zhu Z, Xiao Y, Fan S, Li Y, Guo J, Chen N, et al. Auto-adaptive metastructure for active tunable ultra-low frequency vibration suppression. Int J Mech Sci 2024;271.
[19] A. Yousefi-Koma, J. Sasiadek, G. Vukovich, LQG control of flexible structures using piezoelements, in: Guidance, Navigation, and Control Conference 1994.
[20] Vasques CMA, Dias RJ. Active vibration control of smart piezoelectric beams: comparison of classical and optimal feedback control strategies. Comput Struct 2006;84:1402–14.
[21] Sethi V, Gangbing S. Multimodal vibration control of a flexible structure using piezoceramic sensor and actuator. J Intell Mater Syst Struct 2007;19:573–82.
[22] Niu W, Zou C, Li B, Wang W. Adaptive vibration suppression of time-varying structures with enhanced FxLMS algorithm. Mech Syst Sig Process 2019;118:93–107.
[23] Niu W, Li B, Xin T, Wang W. Vibration active control of structure with parameter perturbation using fractional order positive position feedback controller. J Sound Vib 2018;430:101–14.
[24] Abdeljaber O, Avci O, Inman DJ. Active vibration control of flexible cantilever plates using piezoelectric materials and artificial neural networks. J Sound Vib 2016;363:33–53.
[25] Kassem M, Yang Z, Gu Y, Wang W, Safwat E. Active dynamic vibration absorber for flutter suppression. J Sound Vib 2020;469.
[26] Lu Q, Wang P, Liu C. An analytical and experimental study on adaptive active vibration control of sandwich beam. Int J Mech Sci 2022;232.
[27] Zhang Y, Sun W, Zhang H, Du D, Xu K. Active vibration control of fluid-conveying pipelines: theoretical and experimental studies. Int J Mech Sci 2024;270.
[28] Elliott S, Stothers I, Nelson P. A multiple error LMS algorithm and its application to the active control of sound and vibration. IEEE Trans Acoust Speech Signal Process 1987;35:1423–34.
[29] Oh J-E, Park S-H, Hong J-S, Shin J. Active vibration control of flexible cantilever beam using piezo actuator and Filtered-X LMS algorithm. KSME Int J 1998;12:665–71.
[30] Meng D, Xia P, Song L. MIMOMH feed-forward adaptive vibration control of helicopter fuselage by using piezoelectric stack actuators. J Vib Control 2018;24:5534–45.
[31] Meng D, Xia P, Song L, Smith EC. Experimental study on piezoelectric-stack-actuator-driven active vibration control of helicopter floor structure. J Aircr 2020;57:377–82.
[32] K. Mayyas, T. Aboulnasr, (n.d.). A robust variable step size LMS-type algorithm: analysis and simulations. 1995 International Conference on Acoustics, Speech, and Signal Processing. (1995).
[33] Li W, Wang W, Li B, Yang Z, Irfan M. Error signal differential term feedback enhanced variable step size FxLMS algorithm for piezoelectric active vibration control. Shock Vib 2020;2020:1–10.
[34] Elliot S. Signal processing for active control, ser. Signal Processing and its Applications London: Academic Press; 2001.
[35] Kuo SM, Morgan DR. Active noise control systems: Wiley. N Y 1996.
[36] Snyder SD, Hansen CH. The effect of transfer function estimation errors on the filtered-x LMS algorithm. IEEE Trans Signal Process 1994;42:950–3.
[37] Tobias OJ, Bermudez JCM, Bershad NJ. Mean weight behavior of the filtered-X LMS algorithm. IEEE Trans Signal Process 2000;48:1061–75.
[38] Saito N, Sone T. Influence of modeling error on noise reduction performance of active noise control systems using filtered-X LMS algorithm. J Acous Soc Japan (E) 1996;17:195–202.
[39] Cornelissen D, Sommen PC. New online secondary path estimation in a multipoint filtered-X algorithm for acoustic noise canceling. Proc IEEE ProRIS 1999;99:97–103.
[40] Eriksson LJ, Allie MC. The use of random noise for on-line transducer modeling in an adaptive active attenuation system. J Acoust Soc Am 1986;80. S11 -S.
[41] Bao C, Sas P, Van Brussel H. Adaptive active control of noise in 3-D reverberant enclosures. J Sound Vib 1993;161:501–14.
[42] Kuo SM, Vijayan D. A secondary path modeling technique for active noise control systems. IEEE Trans Speech Audio Process 1997;5:374–7.
[43] Zhang M, Lan H, Ser W. Cross-updated active noise control system with online secondary path modeling. IEEE Trans Speech Audio Process 2001;9:598–602.
[44] Ming Z, Hui L, Wee S. A robust online secondary path modeling method with auxiliary noise power scheduling strategy and norm constraint manipulation. IEEE Trans Speech Audio Process 2003;11:45–53.
[45] Akhtar MT, Abe M, Kawamata M. A new variable step size LMS algorithm-based method for improved online secondary path modeling in active noise control systems. IEEE Trans Audio Speech Lang Process 2006;14:720–6.
[46] Aslam MS, Raja MAZ. A new adaptive strategy to improve online secondary path modeling in active noise control systems using fractional signal processing approach. Signal Process 2015;107:433–43.
[47] Bao C. Comparison of two on-line identification algorithms for active noise control. In: Proc Conf on Recent Advances in Active Control of Sound and Vibration; 1993. p. 38–51.
[48] Eriksson LJ, Allie MC. Use of random noise for on-line transducer modeling in an adaptive active attenuation system. J Acoust Soc Am 1989;85:797–802.
[49] M.T. Akhtar, M. Abe, M. Kawamata, Modified-filtered-x LMS algorithm based active noise control systems with improved online secondary-path modelling, The 2004 47th Midwest Symposium on Circuits and Systems, 2004 MWSCAS`04: IEEE (2004) I-13.
[50] Kwong RH, Johnston EW. A variable step size LMS algorithm. IEEE Trans Signal Process 1992;40:1633–42.
[51] Aboulnasr T, Mayyas K. A robust variable step-size LMS-type algorithm: analysis and simulations. IEEE Trans Signal Process 1997;45:631–9.
[52] Pazaitis DI, Constantinides AG. A novel kurtosis driven variable step-size adaptive algorithm. IEEE Trans Signal Process 1999;47:864–72.
[53] Ang W-P, Farhang-Boroujeny B. A new class of gradient adaptive step-size LMS algorithms. IEEE Trans Signal Process 2001;49:805–10.
[54] Si K. A class of adaptive step-size control algorithms for adaptive filters. IEEE Trans Signal Process 2002;50:1315–26.
[55] Chen W, Lu C, Liu Z, Williams H, Xie L. A computationally efficient active sound quality control algorithm using local secondary-path estimation for vehicle interior noise. Mech Syst Sig Process 2022;168.
[56] K.S. Miller, B. Ross, An introduction to the fractional calculus and fractional differential equations: Wiley, (1993).
[57] A.A. Kilbas, H.M. Srivastava, J.J. Trujillo, Theory and applications of fractional differential equations: Elsevier, (2006).
[58] K. Oldham, J. Spanier, The fractional calculus theory and applications of differentiation and integration to arbitrary order: Elsevier, (1974).
[59] Diethelm K, Ford NJ. Analysis of fractional differential equations. J Math Anal Appl 2002;265:229–48.
[60] Leng J, Xie F, Wu X, Liu Y. Effect of the γ-radiation on the properties of epoxy-based shape memory polymers. J Intell Mater Syst Struct 2013;25:1256–63.